國立臺灣大學電機資訊學院電機工程學系

博士論文

Department of Electrical Engineering

College of Electrical Engineering and Computer Science

National Taiwan University

Doctoral Dissertation

應用呼吸替代訊號與端點對位之肝腫瘤即時追蹤方法

Real-Time Tracking of Liver Tumors by Surrogate Signals and End-Points Registration

張凱翔

Kai-Hsiang Chang

指導教授：陳永耀 博士

Advisor: Yung-Yaw Chen, Ph.D.

中華民國 103 年 7 月

July 2014

誌謝

首先誠摯地感謝指導教授陳永耀博士在這些年中費心地教導，使得我得以一窺電機醫學工程技術領域的深奧，適時地在我迷惘時指點迷津，成為我的人生導師，更是生命中的貴人。我遵循著教授「主動積極，獨立思考」的八字箴言，得以完成博士學業，此成就應歸功於指導教授。本論文的完成亦得感謝臺大機械系顏家鈺教授、臺大醫工所林文澧教授、臺大電機系連豊力教授、臺大醫院何明志醫師與葉啟娟醫師在研究上給我的指導與建議，有您們的協助使得本論文能夠更完整而嚴謹。

感謝智慧型精密運動控制實驗室的學長聲仰、助理郁文以及歷屆的學弟妹們，感謝您們在這幾年來與我互相砥礪、共同成長，這一切銘記在心。最重要的我的父母以及女友鄢如，有您們的支持與鼓勵我才能任性地、安心地完成學業。

研究的旅途中總是苦悶的，唯有不以苦為苦方能成人。

張凱翔 謹致

中華民國 103 年 7 月 於 台灣大學電機工程學系

摘要

腫瘤的定位追蹤在肝腫瘤放射線治療以及熱治療中佔據極為重要的角色，由於肝腫瘤受到呼吸作用影響而在腹腔內產生移動，增加了治療的困難度，所以追蹤精度是影響治療的效率以及安全性的重要因素。本論文提出了兩種追蹤肝腫瘤的方式：(1)呼吸替代訊號追蹤法，以及(2)超音波與斷層掃描影像對位追蹤法。

第一個方法是利用呼吸替代訊號進行肝腫瘤追蹤，其主要概念是利用呼吸替代訊號與肝腫瘤運動之間存在的運動關聯性對肝腫瘤進行位置追蹤。不同於其他追蹤方法，本研究所採用的呼吸替代訊號是體表變化等生理訊號，因此具有非侵入性與即時量測之優點，再者此方法沒有 X 光暴露的疑慮，適合進行長時間的追蹤。本研究以動物實驗之方式確認體外呼吸替代訊號與肝腫瘤運動之關聯性，並且以仿體實驗進行端點定位方法的驗證，結果顯示提出之方法具有良好的準確度。

第二個方法是超音波與電腦斷層影像對位追蹤法，由於肝腫瘤在肝臟內且肝臟外型具有形狀的特殊性，因此提出的方法主要概念是先利用肝臟外型對肝臟位置進行定位，再由肝臟位置與肝腫瘤的相對位置推測出肝腫瘤的位置，以達到肝腫瘤追蹤的目的。本研究提出一種超音波與電腦斷層影像校正技術，提升影像對位速度，改善影像對位時間過長之困難，使其可對肝腫瘤進行即時追蹤。此方法具有其新穎性，並且以仿體實驗進行靜態與動態追蹤的驗證，其結果顯示此方法應用於即時肝腫瘤追蹤的可行性。

本論文提出的兩個肝腫瘤即時追蹤方法，經過實驗驗證皆能對在腹腔內移動的肝腫瘤進行即時的位置追蹤，並且未來可作為位置導引系統應用於肝腫瘤的治療，例如肝腫瘤放射線治療以及熱治療等。兩種方法具有自身的獨特性，可在不同的情況下選擇適合的追蹤方式，極具有臨床研究的潛力。

關鍵字：肝腫瘤追蹤，呼吸替代訊號，醫學影像定位，定位型超音波，影像對位。

Abstract

Tumor tracking plays one of the most important roles in liver tumor treatment, like radiotherapy and thermotherapy. Due to the fact that liver tumors have respiration-induced movements, accurate tracking is the key issue in treatment. Two methods for liver tumor tracking are proposed in this dissertation: (1) surrogate-based tracking with end-points registration and (2) tracked ultrasound tracking with image registration.

A surrogate-based tracking with end-points registration is presented in this dissertation. Abdominal wall displacement as external respiratory surrogate is used to track liver tumor movement, because liver movement has high correlation to surrogate signals. The end-points of tumor movement are determined by CT image registration to build correlation model. Unlike previous tumor tracking methods, the proposed method is non-invasive and real time. Moreover, it is radiation free so that patients are allowed undergoing long-term tracking. An animal experiment has validated the effectiveness of external respiratory surrogates for liver motion estimation, and a phantom experiment has been validated the performance of image registration. It shows a considerably good accuracy for real-time tracking.

A novel tracked ultrasound tracking method involving image registration is proposed in this dissertation, too. In this method, the position of liver tumor is obtained

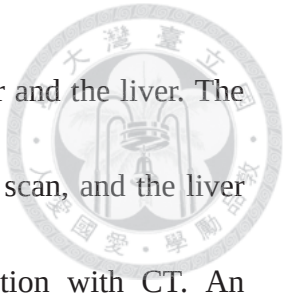

based on liver's position and the relative position between the tumor and the liver. The relative position between the tumor and the liver is obtained by CT scan, and the liver position is determined by tracked ultrasound and image registration with CT. An alignment method is proposed to reduce the run time of image registration for real-time liver tumor tracking. A phantom experiment is conducted, and the results show that the proposed approach has good tracking performance for real-time liver tumor tracking.

The proposed methods have capability to track liver tumor in real time. They have potential to being guidance in radiotherapy or thermotherapy for liver tumor treatment.

Keyword: liver tumor tracking, respiratory surrogate, tracked ultrasound, image registration.

Contents

List of Figures

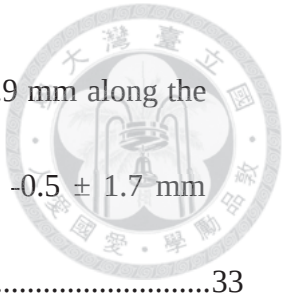

List of Tables

Chapter 1 Introduction

Real-time tracking of liver tumors is focused in this dissertation. It is one of the most important parts in liver tumor treatments, like radiotherapy and thermotherapy. Tracking liver tumor accurately provides correct tumor position to drive treatment devices treating the tumor accurately and efficiently and to protect normal tissues around the tumor from the destruction. Two tracking methods are proposed in this dissertation.

1.1 Motivation and Problem Definition

In the past four decades, liver tumor treatments have been studied extensively because the mortality of liver cancer is almost 10% globally in 2008 (11.3% in male and 6.5% in female) [1, 2] and the 5-year survival rate is only 50-60% after conventional surgical resection [3, 4]. In Taiwan, the mortality of cancer increases by years, and it is 29% in 2013 (29.9% in male, and 27.7% in female) [5]. Furthermore, hepatic carcinoma (liver tumor) is the second among the top ten leading death causes of cancer (18.3% for both sexes, 20.3% for male, and 15.2% for female) [6], as shown in Figure 1.1. It means that one person dies in every hour caused by liver tumor in Taiwan. Liver tumors are a big issue not only in Taiwan, but also in the world.

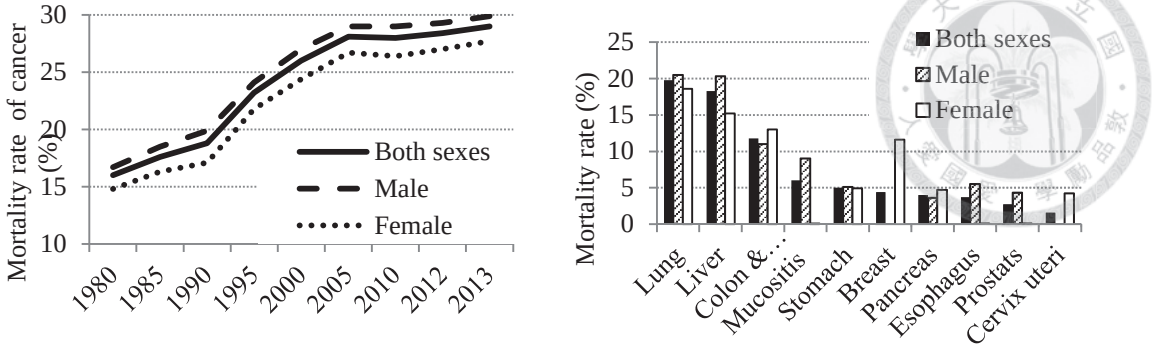

(a) (b)

Figure 1.1 (a) Mortality rate of cancer in Taiwan from 1980 to 2013 [5], and (b) Mortality of the top ten leading cancer in Taiwan 2013 [6].

Treatment options for liver tumors include surgery, chemotherapy, radiotherapy, and thermotherapy. Surgery is unfavorably invasive and with high relapse rate (40% at 5 years) [7, 8]. Chemotherapy is plagued with undesirable side effects and damages to the normal tissues. Radiotherapy and thermotherapy, which are less-invasive, hence have become popular for liver tumor treatment options in recent years [9-16]. Most of non-surgical treatment options have to overcome the issues of localizing tumors and avoiding respiration effect on the liver movement.

Due to two facts, one is that liver is not easily detectable in the abdomen and, while the other is that liver has a respiration-induced movement [17-20], accurate tracking of liver tumors is one of the most important key issues in treatments. Anatomically, the liver is under the diaphragm which is a sheet of muscle separating the chest and abdomen. The diaphragm contracts to draw air into the lungs while inhale; the diaphragm relaxes to expel air from the lungs while exhale, as shown in Figure 1.2.

Liver tumors move in the abdomen due to the action of diaphragm. Furthermore, liver tumors are affected by respiration (Figure 1.3). Tumor movement has variety of types, such as frequency changing, baseline shifting, amplitude changing, etc. [21]. The frequency of liver motion induced by respiration is 0.43 Hz (period: 2.3 second), and the secondary frequency of liver motion due to heartbeat is 1.11 Hz (period: 0.9 second) [22]. The amplitude of liver tumor movement is at the range of 12 and 25 mm [17-21, 23-27], and it leads difficulties of liver tumor treatment. Under inaccurate tracking, treatment dose might not cumulate efficiently for the goal of cancer cells destruction. Moreover, normal tissues around tumors might receive treatment dose and lose their normal function. For these reasons, tumor motion tracking becomes one of the most important issues while treatment, like radiotherapy and thermotherapy.

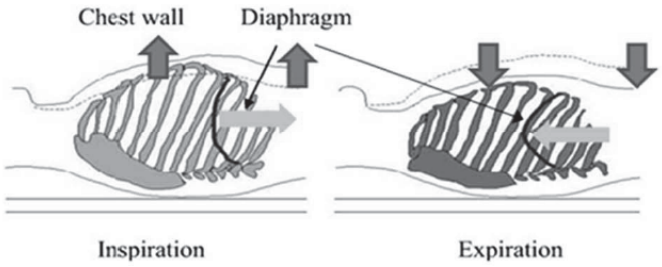

Figure 1.2 Illustration of breathing [28]. While inspiration, diaphragm contracts and drives abdominal wall to move up. While expiration, diaphragm relaxes and makes abdominal wall to move low.

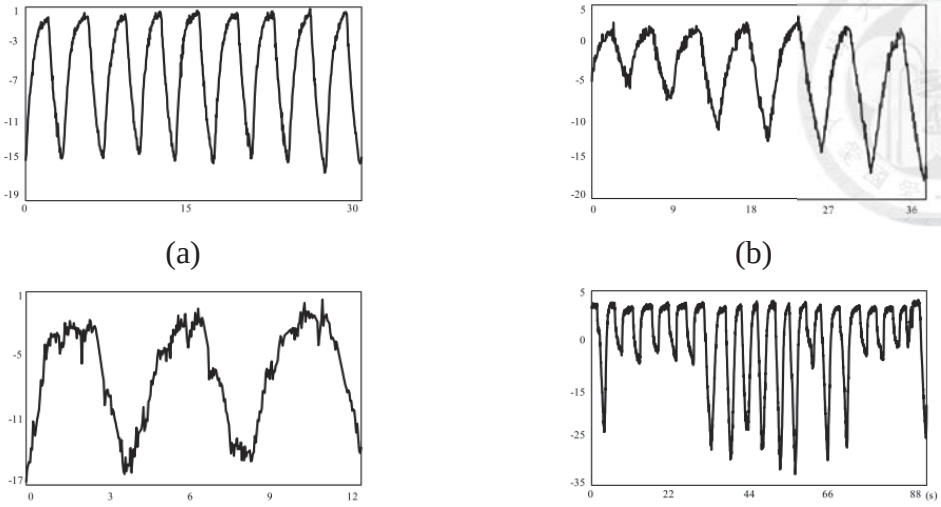

Figure 1.3 A variety of tumor movement. (a) regular breathing, (b) frequency changing, (c) heartbeat effect, and (d) amplitude changing [21].

1.2 Previous Work

To track liver tumors, a number of tracking methods are proposed. They can be categorized into invasive, mini-invasive, and non-invasive. In invasive tracking, active or passive position sensors, like electromagnetic (EM) trackers and radiofrequency identification (RFID) devices, are inserted near the target tumors into human body to determined tumor position indirectly. Biplane X-ray and computed tomography (CT) are mini-invasive tracking methods due to the requirement of markers and radiocontrast agents implantation. Magnetic resonance imaging (MRI) and tracked ultrasound are non-invasive methods of liver tumor tracking using medical image techniques. However, continuous tracking of liver tumor is still not feasible because CT will impose hazardous radiation for a long period of exposure, and MRI has sampling rate lower

than 1 Hz, which is not fast enough for real time tracking [29]. Many therapeutic measures like gating [30-33] and breath-holding [31-34] are therefore applied to remedy this problem. In gating and breath-holding methods, a liver tumor is treated only when it moves into the treating area. Their treatment efficiency is low and the treatment time is long because of their low treatment duty cycle. Tracking is more efficient than gating and breath-holding because a liver tumor could be treated continuously.

1.3 Proposed Approach

To tracking liver tumors in real-time, two tracking methods are proposed: (1) surrogate-based tracking and (2) tracking ultrasound-CT image registration tracking

- **Surrogate-Based Tracking**

Surrogate-based tracking is one of the ways to track liver tumors. The concept of this method is to estimation tumor movement referring the correlation between tumor movement and surrogate signals. Liver tumor motion is known to have high correlation to the motion of diaphragm [35, 36], respiratory volume [32, 33, 37-39], chest [32, 33, 40-43], and abdominal wall [37, 42, 44]. However, there are two main issues of respiratory surrogate-based tracking: effectiveness of the respiratory surrogates and determination of actual tumor position.

In this study, a surrogate-based tacking using abdominal wall displacement to track liver tumors is proposed, shown in Figure 1.4. Liver tumor movement is determined by abdominal wall displacement and the correlation model. The effectiveness of the correlation model is verified via an animal experiment, and the actual tumor position is determined by an end-points registration method.

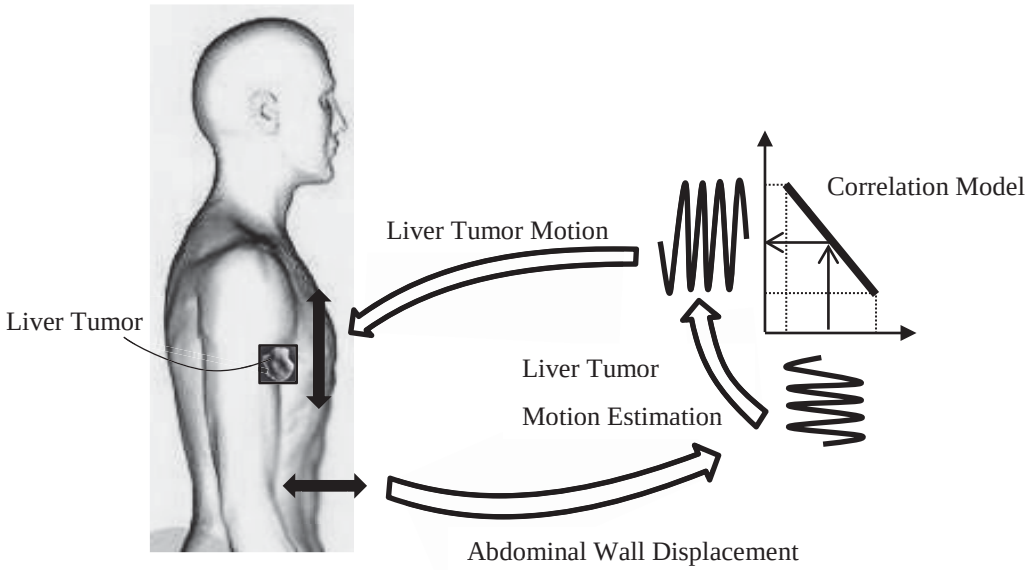

Figure 1.4 Illustration of the proposed approach for liver tumor tracking based on external surrogates. Liver tumor motion is determined by abdominal wall displacement via estimation.

■ **Ultrasound-CT Image Registration Tracking**

Tracked ultrasound can real-time provide lots of information of liver tumors inside human body, including size, contour, and position. However, the information provided from tracking ultrasound is only 2D information of tumors. It is difficult to obtain 3D information of whole tumor in real time. In this study, an ultrasound-CT image registration tracking method is proposed by involved CT with tracked ultrasound to obtain 3D information of tumors, as shown in Figure 1.5. In this method, liver contour is detected by tracked ultrasound, and it is registered with liver contours from CT. After registration, the relative position between tumor and the tracked contour is obtained. Combining the information of the liver contour position and the relative position of tumor, the actual position of tumor could be determined.

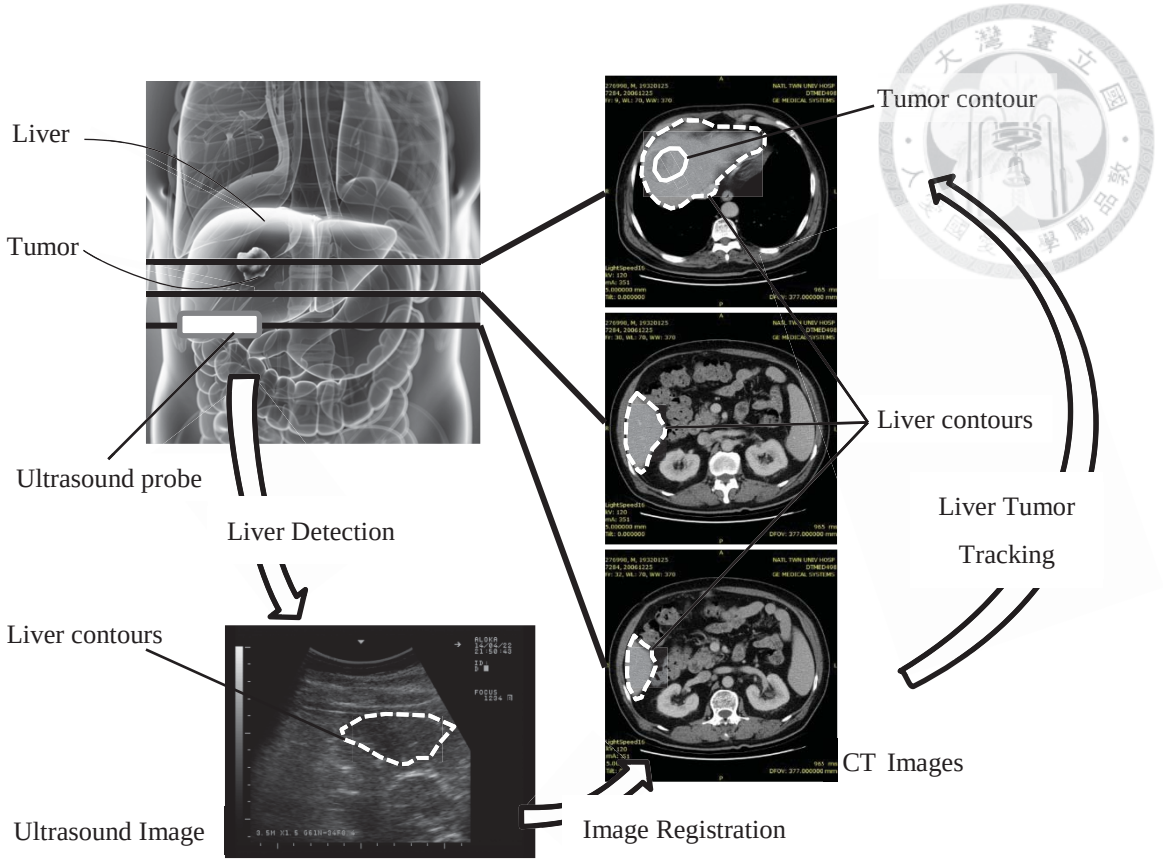

Figure 1.5 Illustration of tracked ultrasound tracking with CT image registration for liver tumor. The concept of this method is to track one of liver's cross section by tracked ultrasound and then to track tumor's position by inferring the relative position between the liver and the tumor from CT information.

1.4 Organization

This dissertation is organized into five chapters. In addition to the background and previous work of liver tumor tracking, Chapter 1 presents the motivation and purpose of this study. Chapter 2 shows a number of existing technologies of tracking are reviewed and summarized. Chapter 3 presents the effectiveness of abdominal wall displacement for liver tumor tracking is verified via an animal experiment and proposes a method to

track the end-points of liver tumor position preoperatively for liver tumor motion model development. Chapter 4 proposes a novel tracking method using tracked ultrasound with image registration. Chapter 5 presents the conclusions and contributions of this work, and the future work is also presented.

Chapter 2 Tumor Tracking Methods

In this chapter, a number of existing methods for tumor tracking are presented. They are categorized into invasive, mini-invasive, and non-invasive tracking methods. In invasive tracking, patient's body is implanted one or more than one tracking sensors, such as electromagnetic tracking systems (also called EM tracker) and radio-frequency identification (RFID) devices, to track target tumors. The sensors are inserted near target tumors and they continuously transmit signal actively or passively in the body. Mini-invasive tracking is a technique to localization target organs using medical image devices, such as X-ray imaging, and X-ray computed tomography (CT), due to the visibility of markers in medical images. These methods require inserting tiny metal markers and radiocontrast agents into patient's body to increase the visibility of target tumors. Unlike invasive and mini-invasive, non-invasive provides tumor tracking without requirement of body injury by cutting or piercing. Magnetic resonance imaging (MRI), tracked ultrasound, and surrogate-based estimation are all non-invasive.

All of the methods presented in this chapter are applied in clinic, and they are introduced in the following sections. The architecture of the organ tracking methods is shown in Figure 2.1. The invasive tracking including EM tracking system and RFID is introduced in Section 2.1. Mini-invasive tracking and non-invasive tracking are reviewed in Section 2.2 and 2.3, respectively.

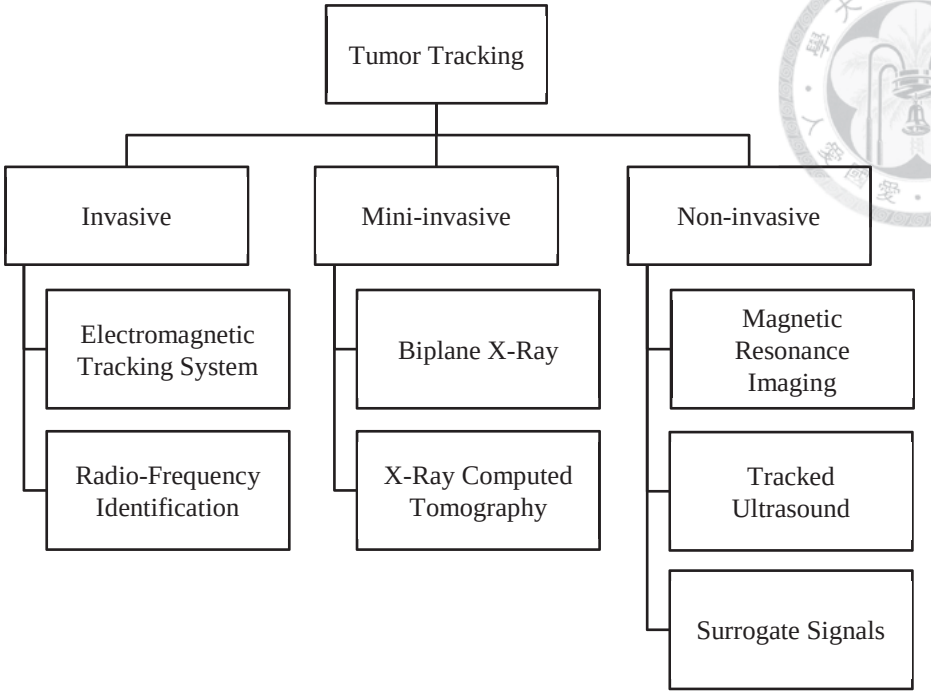

Figure 2.1 Architecture of tumor tracking methods.

2.1 Invasive Tracking

To track moving tumors, spatial tracking sensor insertion is one of the easy and straightforward selections. In 2006 Yaniv and Cleary determined liver motion induced by respiration by implanting electromagnetic sensors of an EM tracking system in the liver [45]. In 2013, Imai *et al.* implanted a miniature wireless RFID tag near lung tumors, which also have movements induced by respiration, for tumor motion monitoring [46]. Tracking by EM tracker and RFID is a direct and real-time liver motion tracking method. However, sensor insertion is invasive, and the implanted sensor should be removed from the body after the treatment. It might lead extension of cancer cells and internal hemorrhage.

2.2 Mini-Invasive Tracking

Biplane X-ray and CT are common methods to track or detect tumor's location in clinic. However, to track tumors accurately, tiny metal markers and radiocontrast agents are essential to be inserted into patient's body due to the low distinguishability of tumors in X-ray and CT images, so these techniques are mini-invasive tracking.

2.2.1 Biplane X-Ray

Biplane X-ray is a technique for diagnosis and tumor tracking. A biplane X-ray system can obtain the 3D location of the target through analyzing the images from two perpendicular X-ray devices, and it has 1 mm accuracy and 30 Hz sampling rate [22, 24, 25, 45, 47]. If the images of tumors are not clear enough, fiducial markers are implanted near the target tumors to increase tracking accuracy. In 2003, Kitamura *et al.* used biplane X-ray to track liver tumors and measured their movements [24]. The tracking accuracy of biplane X-ray for moving liver tumors was validated by Yaniv and Cleary [45], and the tracking accuracy was 0.7 mm. Biplane X-ray is not only used to track liver tumors but also applied in lung tumors tracking. Since 2000, Shirato *et al.* used biplane X-ray to track lung tumors in gated radiotherapy [25, 48, 49]. However, radiation dose is an anxious issue for patients, especially under such a high radiation exposed rate or during long-term exposure. A high radiation dose over a short amount of

time causes radiation sickness, while lower doses can give an increased risk of radiation-induced cancer.

2.2.2 Computed Tomography

Nowadays, CT is a common medical imaging device for diagnosis because it has capability to obtain the 3D anatomic structures of the human body. CT scan is not only applied to 3D reconstruction, but also used for tumor localization. Since 2000, CT is used to track the location of lung tumors, pancreatic tumors, and liver tumors for breathing synchronized radiotherapy as image guidance [33, 50, 51]. A number of researchers not only used CT to track organs but also to measure their masses and deformation [52-55]. 4D CT, high frame rate CT, has been presented for mobile organ monitoring and tracking. The dynamic motion of the internal objects of the body can be seen by 4D CT scan [50, 53, 54]. However, CT scan leads radiation dose issue because of the high frame rate and the long-term radiation exposure. Radiation free imaging devices have been proposed to reduce and avoid the radiation harm for patient.

2.3 Non-Invasive Tracking

Non-invasive tracking allocates tumors without any tissue injury. One of the ways for non-invasive tracking is to detect tumors' image by medical imaging, like MRI and

tracked ultrasound. The other way to track tumor non-invasively is surrogate-based tracking because surrogate signals have certain correlation with liver tumor motion.

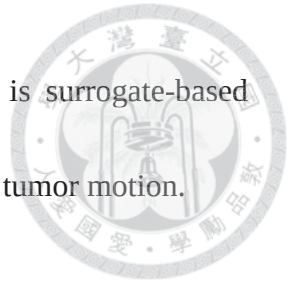

2.3.1 Magnetic Resonance Imaging

In clinic, MRI is applied in organ localization, tumor detection, image-guidance, and temperature monitoring. Since 1999, Shimizu *et al.* measured liver motion using MRI for radiotherapy as guidance [56]. Tokuda *et al.* and Jan *et al.* used MRI-guidance for liver tracking in liver tumor therapy in 2004 and 2007, respectively [57, 58]. A number of researchers determined the movement and the deformation of abdominal organs, like the liver, the prostate, and the uterine fibroids, by MRI [59-61]. Due to its capability of temperature determination, MRI has been used to monitor the temperature change and thermal dose during thermotherapy, such as high-intensity focused ultrasound treatment [62, 63]. However, long scanning time (3.2 seconds per slice) of MRI is one of the limitations for real-time tracking for liver tumors.

2.3.2 Tracked Ultrasound

Tracked ultrasound (also called freehand ultrasound) has been proposed since 1990s. It is a technique combining ultrasound image and spatial tracking techniques to track objects' 3D position. There are two type of tracked ultrasound: electromagnetic-tracked ultrasound [64, 65] and optical-tracked ultrasound [66].

Nowadays, tracked ultrasound is used with CT or MR images for image guidance, called image fusion or image registration, to help surgeons to understand the internal structure of the body. Penney *et al.* tracked liver tumor location using tracked ultrasound and MRI registration during a liver tumor ablation surgery [67]. Mercier *et al.* used tracked ultrasound as intraoperative guidance with MRI image in neuro-navigation system [68]. Tracked ultrasound has advantages of real time imaging, high frame rate, and radiation free. However, tracked ultrasound only provides 2D image information, and this information is not rich enough to track liver tumors which have volume.

2.3.3 Surrogate Signal

Unlike above tracking methods, surrogate-signal-based tracking is a tracking method inferring from the extra information related to tumor motion. It is an indirect tracking method using physiological signals which are related to the tumor motion as surrogates to estimate the movement of tumors. The most commonly used surrogates can be classified into two categories: (1) measurement of the surface displacement of the torso (external surrogates) and (2) measurement of the change of the breathing volume (physiological surrogates). There are correlations between these surrogate signals and liver tumor movements to a certain degree. Comparing with the direct tracking mentioned in the above sections, surrogate-based tracking has a number of advantages: radiation free and high sampling rate.

■ **External Surrogate**

External surrogate signals include the changes of the patient surface, like thoracic and abdominal height. The thoracic and abdominal displacements are caused by respiration, like liver tumors are. The thoracic and abdominal surface moves up and liver tumors move down while inhalation; the thoracic and abdominal surface moves down and liver tumors move up while exhalation. There is a certain correlation between their movements, so the thoracic and abdominal displacements can be a surrogate signal to estimate the movement of liver tumors.

Tsunashima *et al.* used a laser displacement sensor to determine the change of the abdominal height as an external surrogate signal to monitor the location of the liver in 2004 [22]. Gierga *et al.* attached CT visible marker on the abdominal surface and built the correlation model between the abdomen and liver movements [26]. A infrared camera was used to measure the change of the abdominal height to develop the correlation between the liver motion and the external surrogate motion by Beddar *et al.* in 2007 [27]. Wu *et al.* determined the abdominal displacement by attaching an electromagnetic tracking device [69].

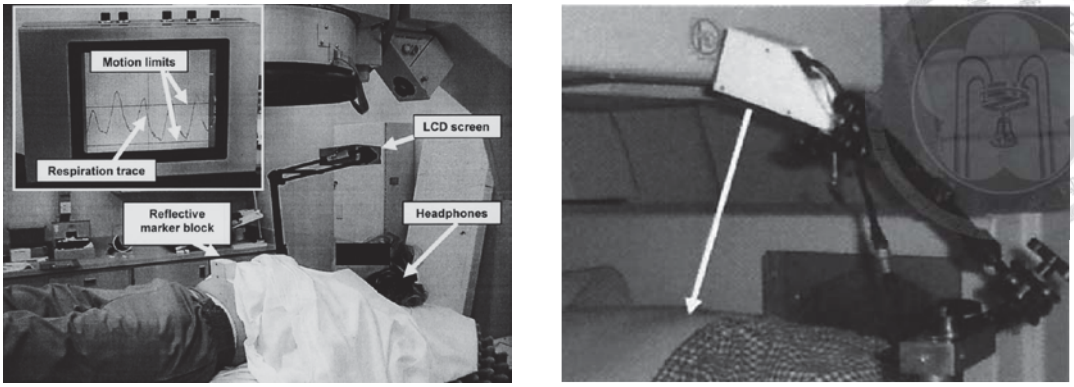

(a) (b)

Figure 2.2 (a) An infrared tracking system is used to measure abdominal displacement [70]. (b) A Laser displacement sensor is placed above a patient to read the displacement of the abdomen [22].

Not only liver tumors, researchers also used the external surrogate signals to estimate lung, pancreatic, and kidney tumors. For lung tumors, thoracic displacement is a useful external surrogate to track or predict their motion because lung tumors are close to the thorax [41, 71, 72]. The change of the abdominal height is also used to track lung tumors since 2000 [22, 33, 37, 73]. Pancreases and kidneys are abdominal organs, so there are certain correlations between their movement and abdominal displacement [26, 33, 74, 75]. In addition, abdominal motion is used to estimate the position of the diaphragm [70, 72] , too.

- **Physiological Surrogate**

All of heart bits, blood pressure, and breathing flow are physiological signals. Because tumor's movement is caused by respiration, breathing related signals can be

surrogates to track mobile tumors. Physiological signals relative to breathing include breathing flow and the change of thoracic perimeter. These signals are breathing related and measureable, so they are chosen to be surrogates for tumor motion estimation.

Kubo and Hill proposed a method using a belt attached a strain gauge to measurement the change of the thoracic perimeter to monitor respiration for gated radiotherapy. The belt was placed around a patient's torso [32]. Spirometers were used to measure respiratory flow to estimate tumor motion by Hoisak *et al.* [37], Kimura *et al.* [39], and Zhang *et al.* [38], as shown in Figure 2.3.

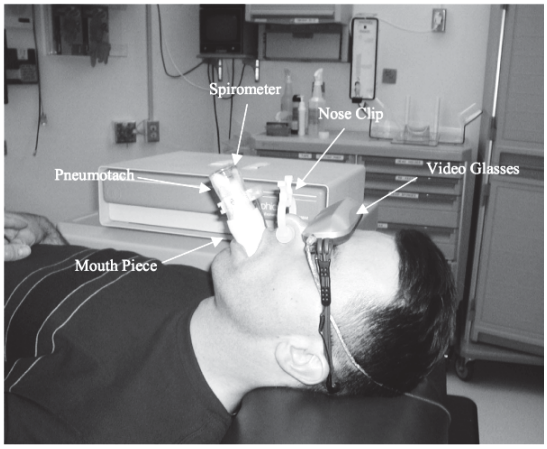

Figure 2.3 Spirometer-based respiratory motion monitoring system [38]. A patient breathes through a mouthpiece with a spirometer, and a nose clip is used to make sure whole breathing is measured by the spirometer.

2.4 Discussions and Summary

In summary, the mentioned methods have capability to track liver tumors in clinical due to their won characteristics. EM and RFID sensors provide real-time and accurate results of tumor tracking, but they are invasive and plagued with undesirable insertion and fearfulness. Biplane X-ray and CT can track tumors accurately by inserting tiny metal markers and radiocontrast agents. Unfortunately, radiation dose effect and low frame rate are two big issues of direct tracking methods for liver tumors which have movements induced by respiration. MRI is radiation free and presents good image quality of tumors, but it cannot maintain real-time tracking for liver tumors due to its low frame rate. Tracked ultrasound can track tumor position and rebuild tumor 3D image. However, it cost long time for 3D reconstruction. Compared with above methods, surrogate-based tracking has three main advantages: safe, real time, and non-invasive.

Table 2.1 Comparison of tumor tracking methods.

Method		Pros	Cons
Invasive	EM tracker	High sampling rate	Cable insertion
	RFID	High sampling rate	Radio interference
		Wire less	Tag insertion
Mini-invasive	Biplane X-ray	High frame rate	Radiation exposure
	CT	3D image	Radiation exposure
		Large FOV*	Low frame rate
Non-invasive	MRI	3D image	Low frame rate
		Radiation free	
		Large FOV*	
	Tracked ultrasound	Portable	Small FOV*
		Radiation free	2D image
	Surrogates	Easy to attach	Arrangement
		Real time	

* FOV: field of view

Chapter 3 Surrogate-Based Tracking with End-Points Registration

In this chapter, a surrogate-based tracking for liver tumor is proposed. It consists of end-points registration and surrogate-tumor movement correlation model development. The proposed approach description is presented in Section 3.1. End-points registration method is verified via a phantom experiment in Section 3.2, and the effectiveness of surrogate model is analyzed via an animal experiment in Section 3.3. A summary is presented in Section 3.4.

3.1 Proposed Approach

To allocate liver tumors, an efficient and accurate tracking method is essential. The causation of liver tumor motion is action of diaphragm. It drives liver and liver tumor to move in abdomen, and the motion of liver causes a number of physiologic signals, like abdominal wall displacement and respiratory flow change. These physiologic signals could be external surrogate signals for liver tumor tracking because they are causal. In this study, a method based on external surrogate signals and assisted by end-points registration is proposed. Liver tumors position and the displacement of abdominal wall are measured to determine the relationship of them. Then, the relationship is used to

track the tumor motion with surrogate signals. This method is also called estimation.

There are two stages of proposed surrogate-based tracking: correlation building (off-line or preoperative) and liver tumor tracking (on-line or intraoperative), as shown in Figure 3.1. In the preoperative correlation building stage, the position of the liver tumor and the height of the abdominal wall are determined by end-points registration and EM tracking system, respectively, in certain breathing stages, such as end of exhalation and end of inhalation. The displacement data of the liver tumor and abdominal wall are used to build the correlation model between of them, as an estimation model. In the intraoperative tracking stage, the displacement of the liver tumor is estimated by the abdominal displacement mapping via the correlation model. The estimated liver tumor displacement will be the spatial information of the target tumor for treatment devices.

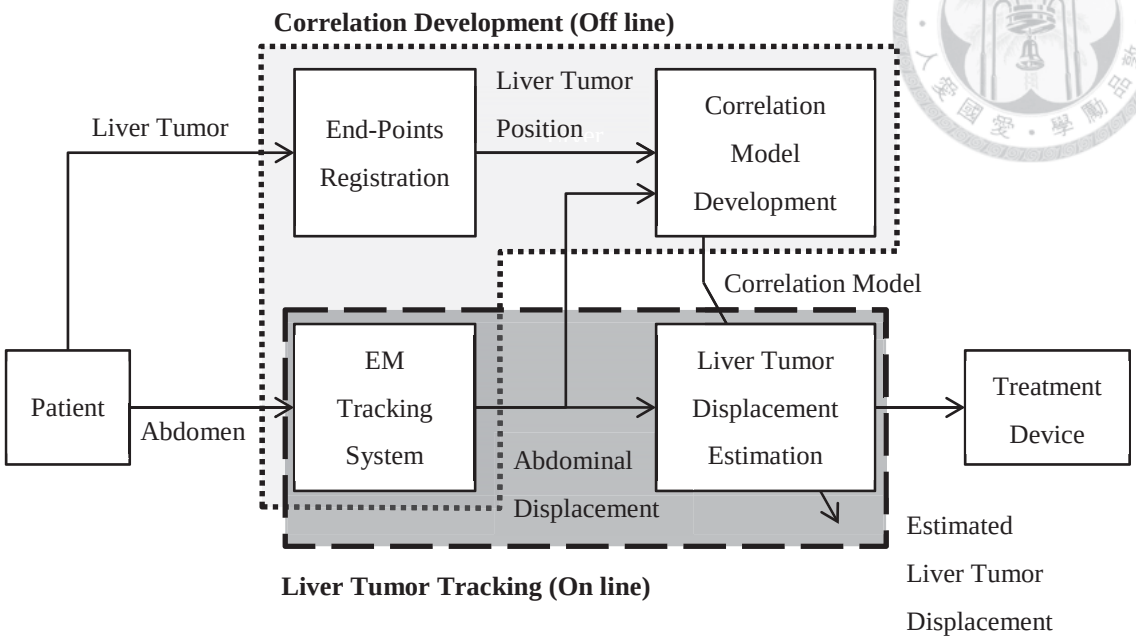

Figure 3.1 Block diagram of surrogate-based tracking with end-points registration for liver tumor tracking.

3.2 End-points Registration

To detect the end-points of tumor movement, an image-to-physical registration using external markers is proposed in this section. Moreover, a phantom experiment is conducted to verify the proposed approach.

3.2.1 Image-To-Physical Registration Using External Markers

Medical image, including CT and MRI, is a common method to localize objects in human body. In 1990s, researchers had used CT to localize organs directly, and the

localization accuracy were around 1 mm for 512 matrix CT images and 2 mm for 256 matrix CT images[76, 77]. However, these localizations were based on CT coordinate system, meaning the localization accuracy is a relative accuracy. If CT image is integrated to other devices, like treatment devices, they should be tracked based on CT coordinate system. It is difficult to operate. In 2011, Mercier proposed a method to integrate MRI image (3D image like CT image) to physical space, called image-to-physical registration [68]. To locate the end-pints of tumor movement, an image-to-physical registration is proposed

There are two main types in image-to-physical registration: anatomical landmarks [68] and artificial markers. In landmark-based registration, anatomical landmarks, including bone, nose, and vessels, are used to develop the transformation from the CT to the US coordinate. The performance of registration is affected by the identification of the markers. Artificial-marker-based registration is to determine the actual tumor position using artificial markers attached inside or outside of human body, as shown in Figure 3.2. In CT images, the position of tumor and markers can be identified, and the position of tumor related to the markers can be determined. The relative position of tumor can map to the physical coordinate system, and then the actual position of tumor can be determined by this spatial information.

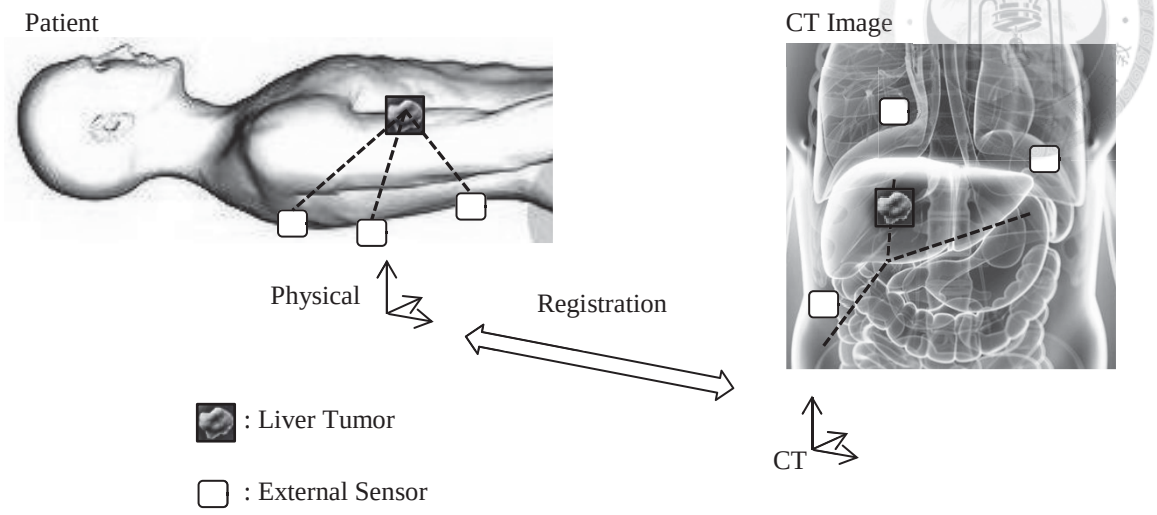

Figure 3.2 Illustration of image-to-physical registration.

Artificial-marker-based registration can be divided into internal and external marker-based. In internal marker-based registration, internal markers are implanted into human bodies. The markers can be close to the target tumor, but it is invasive. Oppositely, external markers are attached to the surface of human body, like chest, abdomen, and the patient's back. It is a non-invasive method.

An image-to-physical registration using external artificial markers is proposed to determine liver tumor's actual position. Three EM tracking sensors (trakSTAR) as external markers are attached to the patient's back, which has no respiration effect during regular breathing. An EM senor is attached on patient's abdomen as an external surrogate. While a patient undergoes CT scan, he/she is asked to stop breathing in two certain breathing stages: end of exhalation (EoE) and end of inhalation (EoI). Tumor

positions in these two breathing stages, which are the end-points of tumor movement, are determined via image-to-physical registration, and the position of external surrogate is also determined via image-to-physical registration. The end-points information of tumor and external surrogate is used to develop the correlation model mentioned in Chapter 3 for liver tumor real-time tracking, as shown in Figure 3.3.

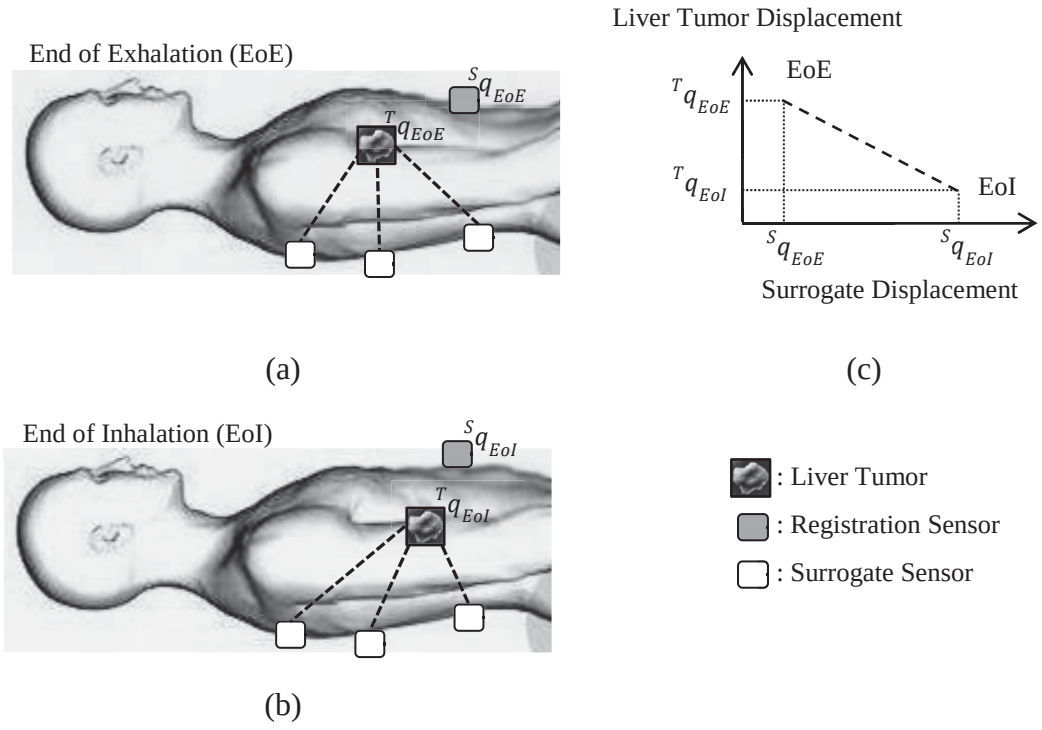

Figure 3.3 Illustration of end-points registration applied to surrogate-based liver tumor tracking. (a) Tumor and surrogate position in end of exhalation, (b) Tumor and surrogate position in end of exhalation, and (c) end-points of tumor and surrogate.

In order to determine the actual position of tumors in physical coordinate system (world space), the CT image should be transferred to the world space, which is the EM coordinate system in this study. This technique is coordinate transformation, also known

as image-to-physical registration. The transformation from the CT to the world coordination can be obtained by calculating the relationship of markers in the two sets of coordinates.

After obtaining the relationship, objects in the CT image can be mapped from CT space into the world space by the following formulation:

$$^{W}q = {}^{W}T_{CT} \cdot {}^{CT}q \tag{1}$$

where ^{CT}q and ^{W}q are the object coordinate in CT and world space, respectively, and registration matrix, $^{W}T_{CT}$, is a 4×4 transformation matrix from CT to the world space. Registration matrix is determined using the position of sensors (markers) in image (CT) and physical (world), called image-to-physical registration. The transformation of sensors in CT and sensor space can be written as the following formula:

$$^{W}q_s = {}^{W}\begin{bmatrix} q_x & q_y & q_z & q_{org} \\ 1 & 1 & 1 & 1 \end{bmatrix}_s = {}^{W}T_{CT} \cdot {}^{CT}\begin{bmatrix} q_x & q_y & q_z & q_{org} \\ 1 & 1 & 1 & 1 \end{bmatrix}_s = {}^{W}T_{CT} \cdot {}^{CT}q_s \tag{2}$$

where $^{CT}q_s$ is the sensor coordinate in CT space, and $^{W}q_s$ is the sensor coordinate in world space read by EM tracker. Three sensor coordinates are identified as q_{org}, q_x, and q_y, which are read from the tracking system. q_z is the vector from cross product of $q_x - q_{org}$, and $q_y - q_{org}$. The coordinate set of three sensors, ^{CT}q, is square full-rank matrix, so it is invertible. The registration matrix, $^{W}T_{CT}$, can be obtained by

right multiplying inverse of the coordinate set in CT as (3).

$$^{W}T_{CT} = {}^{W}q_s \cdot \left({}^{CT}q_s\right)^{-1} \quad (3)$$

3.2.2 Experiment Design

In the CT image, liver has different intensity than other tissues in gray scale, and it is displayed in gray. Moreover, the fat is displayed in dark shades whereas bones are displayed in white (Figure 3.4 (a)). In order to verify the performance of the proposed method, an *in vitro* phantom is made for the experiments. The phantom which consists of a pig liver fixed in a tank filled with agar and four tracking sensors that serve as references was used in this study, as shown in Figure 3.4 (b). Three external sensors are arranged under the phantom, as shown in Figure 3.4 (c). In the CT image, the phantom is displayed in varied intensity due to the difference in their X-ray absorption (Figure 3.4(d)). The pig liver and agar are displayed in different shades of gray. The agar has uniform texture and less echo-reflective, so its area appears dark. Tracking sensors have highest absorption, so they appear as white in the CT image. The position of the sensors is clearly visible. The coordinates of external sensors are used for image-to-physical registration, and the coordinates of reference sensors are used to validate the tracking performance of CT localization.

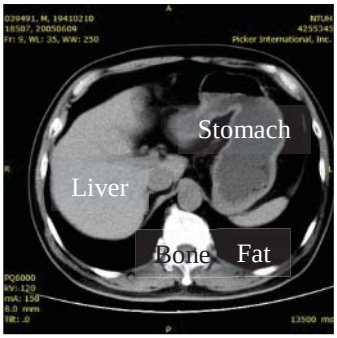

(a)

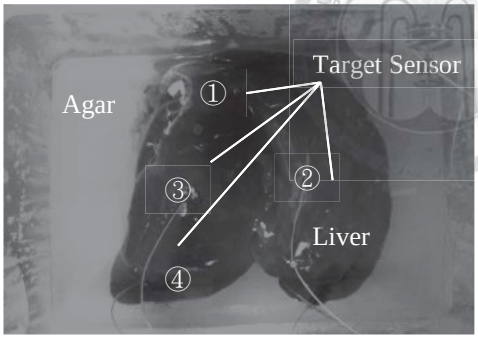

(b)

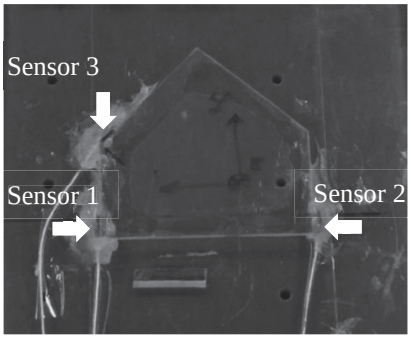

(c)

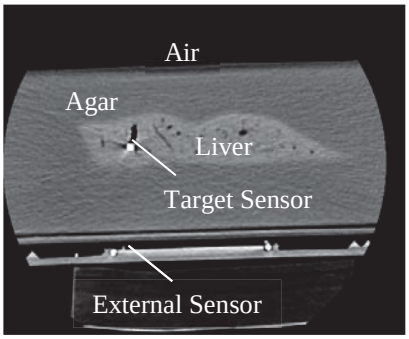

(d)

Figure 3.4 (a) CT image of human abdomen, (b) Phantom which consists of a pig liver fixed by agar with the arrangement of the reference sensors, (c) arrangement of external sensors, and (d) the CT image of *in vitro* phantom including liver, agar, and sensors.

The experiment was conducted with three phantoms to verify the performance of proposed registration method. Four sensors were attached into pig livers as targets (references). The experiment was repeated five times for purpose of data collection. The registration is to determine the relationship between the CT image and physical space, and then the object coordinates can be transferred using the relationship, as shown in Figure 3.5. The spatial information of external sensors in CT and physical are used to

determine the registration matrix which is the relationship from CT image to physical space. After obtaining the registration matrix, the coordinates of external sensors are transferred from CT into physical space. The difference between the external sensors before and after registration is the registration error. The coordinates of references in CT are also transferred into physical space using the registration matrix, and the differences between the references before and after registration is the validation error.

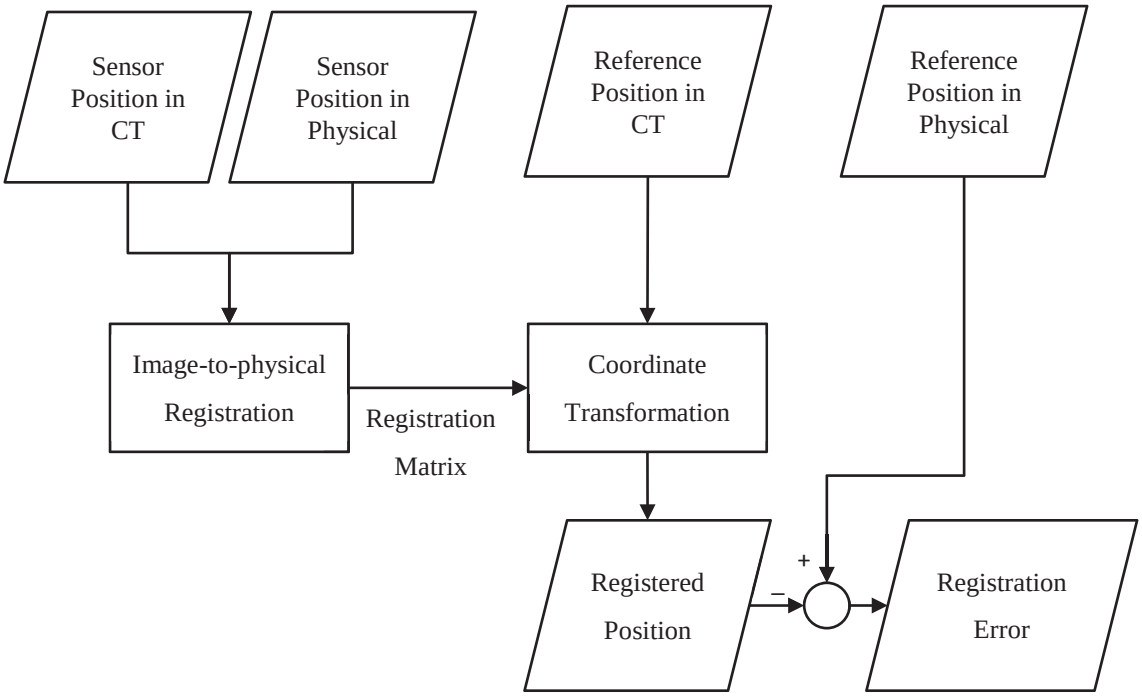

Figure 3.5 Flow chart of CT-to-physical registration.

3.2.3 Experiment Results and Discussions

The registration error is established as 2.07 ± 0.73 mm (mean ± STD) for $N = 60$ (1.91 ± 0.34 mm in case 1, 1.81 ± 0.70 mm in case 2, and 2.51 ± 0.85 mm in case 3),

shown in Figure 3.6. The range of error is from 1.00 to 3.82 mm. The errors are -0.3 + 1.9 mm along the CC-dir., -0.3 ± 0.9 mm along the AP-dir., and -0.5 ± 1.7 mm along the LR-dir., respectively (shown in Figure 3.7).

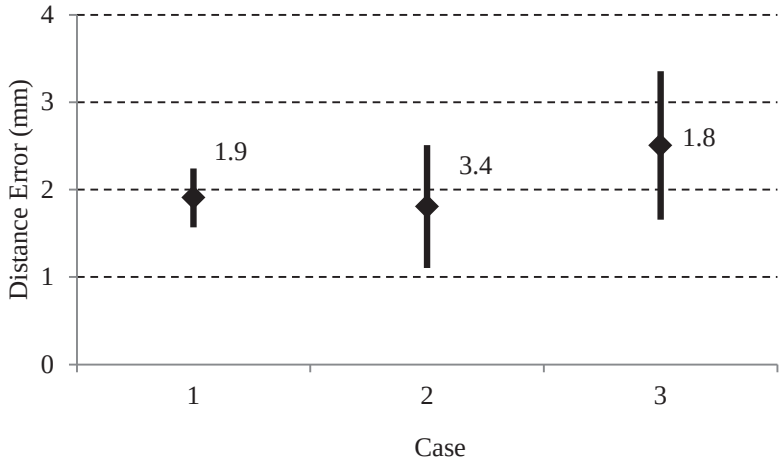

Figure 3.6 Results of CT-to-physical registration in each case. Registration errors are 1.91 ± 0.34 mm in case 1, 1.81 ± 0.70 mm in case 2, and 2.51 ± 0.85 mm in case 3.

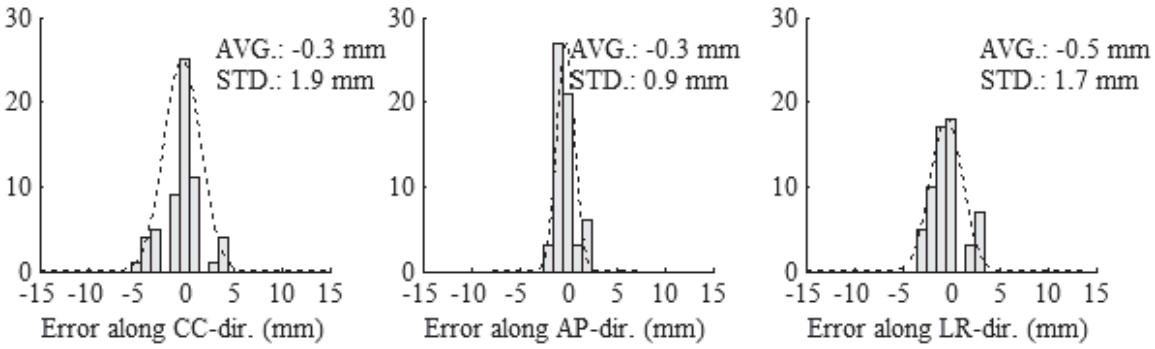

(a) (b) (c)

Figure 3.7 The CT registration error along three axes: (a) -0.3 ± 1.9 mm along the CC-dir., (b) -0.3 ± 0.9 mm along the AP-dir., and (c) -0.5 ± 1.7 mm along the LR-dir..

The image-to-physical registration error is 2.07 ± 0.73 mm. It is supposedly caused by misalignment and low slice resolution. The reason that the CT registration had large STD errors is supposedly that the position of the external sensors may show a degree of inaccurate detection due to the large intervals (1 mm) of the CT slices. It can be enhanced by decreasing the CT interval and reducing the size of the external sensors to advance the accuracy of the CT registration.

In 2011, Mercier *et al.* proposed an MRI-to-patient method using anatomic landmarks [68]. The patient was fixed on a table which was calibrated with an optical tracking device, and the selected landmarks were localized by the optical tracking device. The registration error was 4.9 ± 1.1 mm. Lang *et al.* present a registration method using biplane X-ray and metal marker, and registration error was 2.9 ± 0.8 mm [78]. In our work, the registration error using CT and external marker is 2.07 ± 0.73 mm. The comparison is shown in Table 3.1 Comparison of image-to-physical registration results.. It shows that artificial markers provide better performance than landmarks due to the difficulty of landmark identification. The registration proposed in this study provides better performance, and it can use both CT and MRI image information for difference situations.

Table 3.1 Comparison of image-to-physical registration results.

	Registration	Marker type	Accuracy
Mercier *et al.* [68]	MRI-to-physical	Landmark	4.9 ± 1.1
Lang *et al.* [78]	X-ray-to-physical	Artificial marker	2.9 ± 0.8
Our work	CT-to-physical	Artificial marker	2.07 ± 0.73

Average ± STD (Unit: mm)

3.3 Liver-Surrogate Movement Correlation Model

The method to discuss the effectiveness of liver motion estimation by external respiratory surrogates is proposed in this section, and the correlation model between the liver and external respiratory surrogates movement is obtained via animal experiments. Three main issues are studied: (1) sensor arrangement, (2) multiple sensor fusion, and (3) effective time period. In order to investigate these issues, a liver motion estimation method based on external respiratory surrogate signals retrieved from animal experiment is proposed. In addition to the animal experiments, experimental procedure, and the correlation model regression method, the following sections will propose an approach using external respiratory surrogates to estimate the liver motion.

3.3.1 Liver Motion Estimation Procedure

The proposed liver motion tracking consists of two stages, the model-fitting stage and the motion estimation stage. In the first stage, the movements of the liver and the chest/abdomen are measured separately to establish their correlation model. In the second stage, liver motion is estimated by the chest/abdomen motion as the external respiratory surrogate signals with the previously derived correlation model. The process of liver-motion estimation is shown in Figure 3.8.

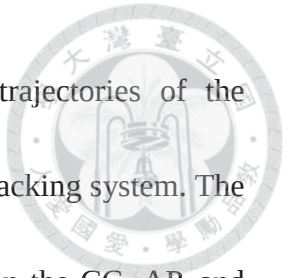

In the model-fitting stage, the input data are the motion trajectories of the chest/abdomen and the liver read from an electromagnetic position tracking system. The liver motion signals are measured from the movement of the liver in the CC, AP, and LR directions. The surrogate signals are measured from the movement of the chest/abdomen in their main motion direction (AP-direction). The correlation between the surrogate and liver motion is then modeled via linear regression method.

In the motion estimation stage, the correlation model obtained from the first stage is incorporated with the external surrogate signals from the chest/abdomen motions to obtain the motion estimation of the targeted liver. Estimation error is identified as the difference between the measured liver motion and the estimated liver motion.

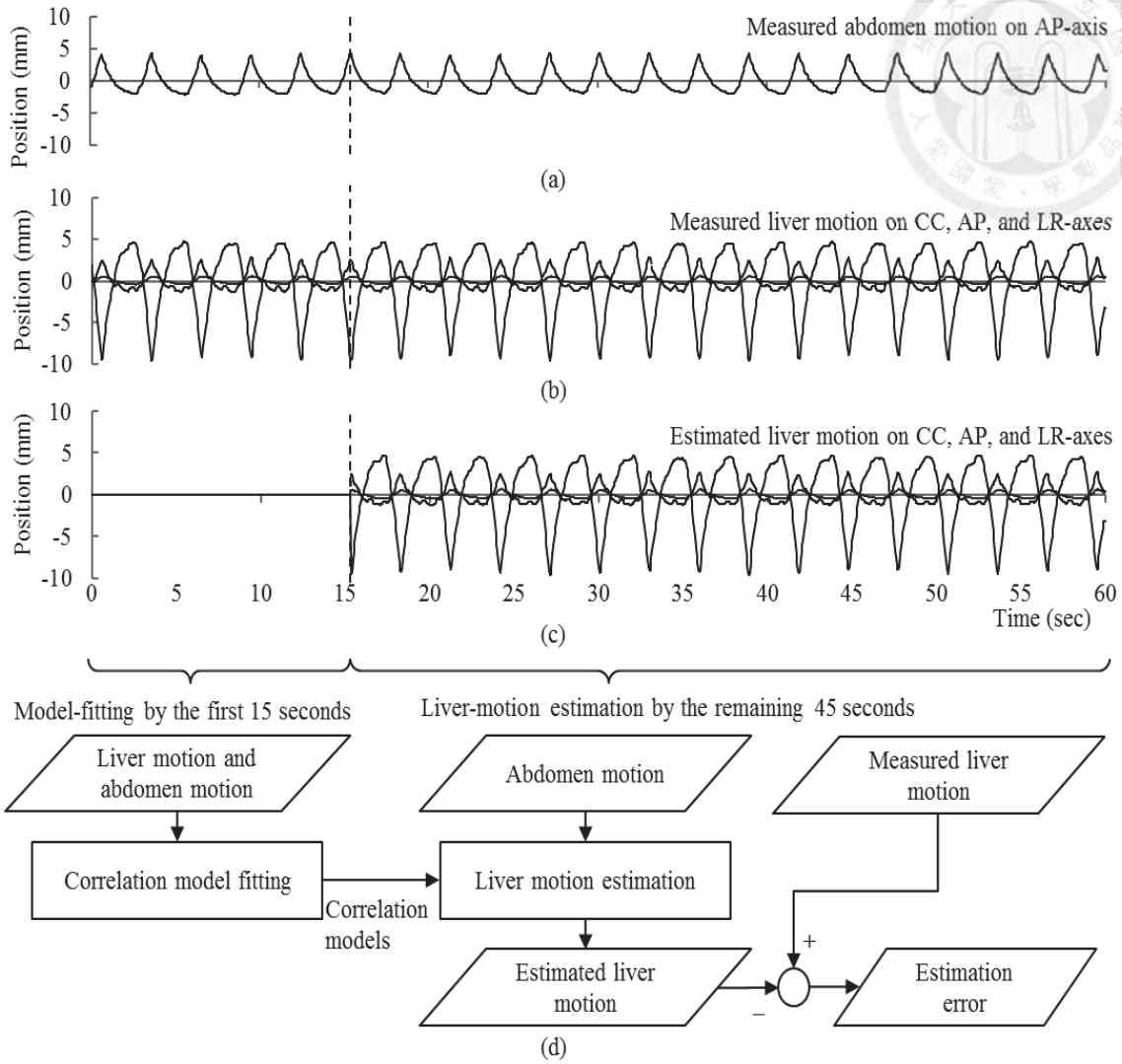

Figure 3.8 Illustration of liver tumor motion estimation using external surrogate signals. (a) Measured abdomen motion on the AP-axis. (b) Measured liver motion on the CC, AP, and LR-axes. (c) Estimated liver motion on the CC, AP, and LR-axes. (d) Flow chart of the liver-motion estimation approach. The first stage is model-fitting; the second stage is liver-motion estimation. Estimation error is the difference between the measured liver motion and the estimated liver motion.

3.3.2 Animal Experiment Design

This section proposes the design and procedure of the animal experiments. The chest/abdomen motion, which is measured by a position tracking sensor, is used as the external respiratory surrogates to estimate liver motion. Other position sensors are surgically attached to the liver of pigs so that actual liver motion can be measured accurately. The signals from external surrogates and actual liver motion are then analyzed. Furthermore, multi-sensor fusion problem is also discussed.

■ **Animal Experiment Hardware Setup**

To estimate liver motion by external respiratory surrogates, correlation model between the liver motion and the surrogate signals was required. Animal experiments were therefore designed to acquire the necessary liver motion and the surrogate signals. Surgeons at National Taiwan University Hospital conducted the animal experiments using six female pigs (weight: 30 kg, length: 1 m) and electromagnetic tracking system.

Based on the anatomic landmarks of the liver, three tracking sensors were designed to attach to the inferior vena cava (IVC), the lower tip of right medical hepatic lobe (TRL), and the lower tip of left lateral hepatic lobe (TLL) respectively (Figure 3.9). Surgeons could identify these locations easily. To identify the liver motion, three axes were used to represent three main axes in the body: the cranial-caudal direction

(CC-direction), the anterior-posterior direction (AP-direction), and the left-right direction (LR-direction) (as shown in Figure 3.9).

To measure the movement of the chest and the abdomen, twelve surrogate locations were chosen for sensor arrangement. The layout of the sensor arrangement was based on a grid on the chest and abdomen in Figure 3.9. The vertical line between the xiphoid process and the pubis was drawn firstly and then was divided into four quarters. The upper bound of the grid was the horizontal line passing through the xiphoid process (C1-C3, represented the movement of lower chest). Two horizontal lines between the upper and lower bound fell on the one quarter (A1-A3, represented the movement of upper abdomen) and the middle (A4-6, represented the movement of middle abdomen).The lower bound was the horizontal line passing through the three quarters (A7-9, represented the movement of lower abdomen). The right and left bounds of the grid were the vertical lines passing through the middle of the right-side and the left-side clavicles. The twelve intersections on the grid were the surrogate points, numbered from right to left and from top to bottom. Due to the anatomical structure of chest and abdomen, the points were labeled “C” for the chest group and “A” for the abdomen group. Surrogates C1 to C3 were on the lower chest, A1 to A3 were on the upper abdomen, A4 to A6 were on the middle abdomen, and A7 to A9 were on the lower abdomen. Electromagnetic sensors were attached to the surrogate points to measure the

chest and the abdomen motion. The electromagnetic transmitter was located on the right-side of pigs near the upper abdomen.

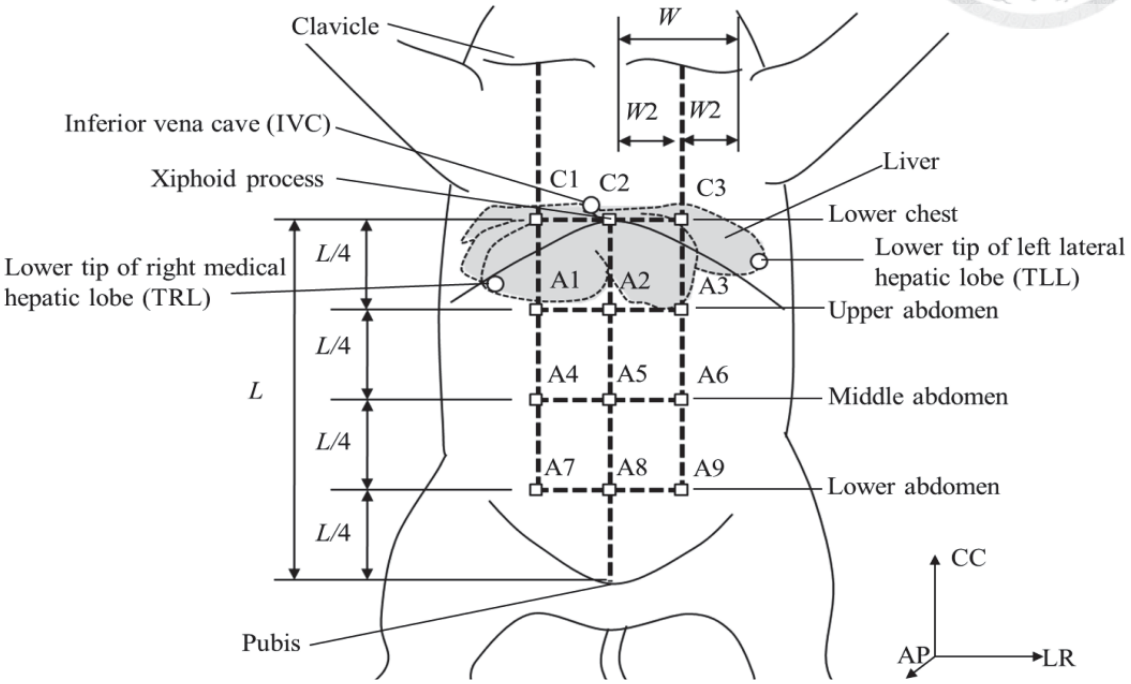

Figure 3.9 Sensor arrangement for animal experiment. The location of trakSTAR sensors on the pig liver (IVC, TRL, and TLL) and the chest/abdomen (C1 to A9). The AP-LR-CC coordinates are shown in the lower right corner.

■ Animal Experiment Procedure

The experiments were conducted with six pigs under general anesthesia. Three pigs were used for the single-surrogate measurement, and the other three pigs were used for the multi-surrogate measurement and the long-term measurement. The sensors were fixed on the landmarks of the liver by surgeons. To avoid any extraneous effects of the operation, the data were acquired on the second, the fifth, and the seventh day after the

sensor-implant operation. All of them breathed with a respirator during measurement.

There were three animal experiments: single-surrogate measurement, multi-surrogate measurement, and long-term measurement. The result of the single-surrogate measurement was used to analyze the sensor arrangement. Multi-surrogate measurement was used to analyze the benefits of the multiple surrogates. Long-term measurement was used to verify the most effective time period.

In single-surrogate experiment, the goal was to estimate the liver motion by analyzing the best location on the chest or abdomen for external respiratory surrogate arrangement. After surgically fixing sensors at IVC, TRL, and TLL of the liver, one other sensor was attached to the chest or abdomen as the surrogate sensor for motion measurement. The motion measurement was performed for one minute for each location from C1 to A9 sequentially, which would be used as the external surrogate in liver motion estimation later. The measurements of three sensors on the liver were performed simultaneously. The derived data include the external surrogate position and the movement of the liver at three locations (IVC, TRL, TLL). The first 15 seconds of the data was used to model the correlation between the liver motion and the external surrogate motion, and the remaining 45 seconds of the data was used to test the accuracy of the proposed liver motion estimation. The estimation results were also used to determine the best location for external respiratory surrogates.

In multi-surrogate measurement, three sensors were attached to IVC, TRL, or TLL to record the liver movement, and three sensors were attached to the chest and the abdomen. Two of the external sensors were fixed on the location of surrogate A2 and C2 based on the finding of the single-surrogate measurement. Surrogate A2 had the best estimation accuracy, while surrogate C2 was at the Xiphoid process and was considered to be the pilot point of the sensor arrangement. Therefore, surrogate A2 and C2 were selected to combine with other surrogates to test the validity of the multi-surrogate model for liver motion estimation. The third sensor was switched from C1 to A9 sequentially. Each measurement was performed for one minute. Each data set was used to determine the correlation model with multi-surrogate and to analyze the benefits of multi-surrogate estimation.

In long-term measurement, the sensor arrangement is basically the same as the previous ones except the external surrogate is at the C2 point only. The first 15 seconds data were also used to estimate the remaining liver motion. The long-term estimation liver movement would be produced via an established correlation model. This measurement was conducted to test the reliability of the correlation model for long-term estimation.

3.3.3 Liver and Chest/Abdomen Movement Analysis

The movements of liver, chest, and abdomen are measured through electromagnetic sensors. The measured data are three-dimensional in the CC, AP, and LR directions. This section shows the characteristics of the signals obtained from the experiments. It also shows the type of the correlation model between the liver and the chest/abdomen movement via a regression method.

■ **Characteristics of Liver Movement**

The liver motion is measured by the electromagnetic position tracking system in the animal experiments. The trajectories have similar patterns and are almost periodic. Figure 3.10 shows the liver motion signals of IVC, TRL, and TLL in the CC, AP, and LR directions measured. The trajectories have frequencies around 0.35Hz with main movements in the CC-direction, minor movements in the AP-direction, and the least movements in the LR-direction. It shows that IVC has larger displacement than TRL and TLL. Table 3.2 shows the average amplitude and standard deviation of the liver movement for 6 pigs during 7 days. For IVC, the average amplitude in the CC-direction is 11.68 mm, and the amplitudes range from 9.14 mm to 12.85 mm. In the AP-direction, the average amplitude is 3.90 mm and the amplitudes are in the range from 2.66 mm to 5.27 mm. The smallest displacement is observed in the LR-direction, where the average

amplitude is 1.39 mm, ranging from 1.03 mm to 1.93 mm. The movements of TRL and TLL are similar to IVC, but their amplitudes are smaller than IVC. The average amplitude of TRL is 7.12 mm in the CC-direction, 1.92 mm in the AP-direction, and 0.96 mm in the LR-direction. The average amplitude of TLL is 7.20 mm in the CC-direction, 2.70 mm in the AP-direction, and 1.81 mm in the LR-direction.

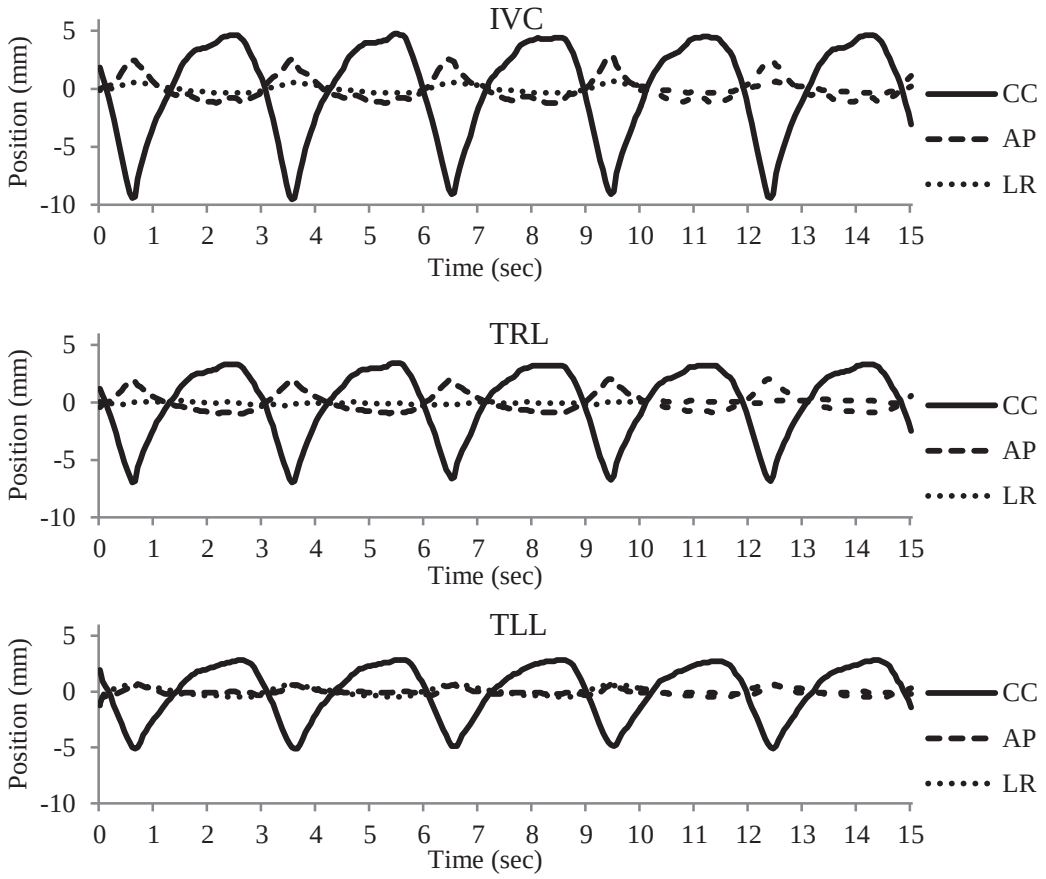

Figure 3.10 Liver movement at IVC, TRL, and TLL. Main movement is in the CC-direction, and second main movement is in the AP-direction. Movement in the LR-direction is less than in the CC and AP directions. Movement at IVC is larger than at TRL and TLL.

Table 3.2 Average amplitude and standard deviation of liver motion in different days for 6 pigs, and the breathing frequency of each pig.

Liver location	Displacement (mm)	Pig 1	Pig 2	Pig 3	Pig 4	Pig 5	Pig 6
IVC	CC	10.6/0.34	12.47/1.68	12.85/0.92	12.81/1.04	9.14/0.74	12.20/0.79
	AP	2.66/0.51	4.34/0.49	3.27/0.55	5.27/0.83	3.09/0.16	4.76/0.89
	LR	1.91/0.57	1.21/0.69	1.03/0.70	1.18/0.71	1.10/0.96	1.93/1.49
TRL	CC	5.16/0.24	6.28/1.08	9.41/0.68	8.11/1.20	5.71/0.27	8.02/1.59
	AP	1.48/0.48	3.04/0.69	2.34/1.00	1.75/1.12	0.56/0.32	2.36/0.42
	LR	0.75/0.40	1.74/0.26	0.44/0.06	1.34/0.58	0.72/0.55	0.77/0.26
TLL	CC	5.51/0.23	7.31/1.13	7.55/0.29	9.29/1.60	5.33/1.35	8.21/1.00
	AP	3.42/0.85	4.20/0.40	1.06/0.22	2.98/0.38	3.07/0.77	1.46/0.54
	LR	1.75/0.50	1.58/0.63	1.41/0.46	2.52/0.18	1.67/1.23	1.91/0.49
Frequency (Hz)		0.39/0.01	0.34/0.06	0.33/0.02	0.34/0.00	0.34/0.00	0.34/0.00

Average/SD

■ **Characteristics of External Surrogate Signals**

The motion of chest/abdomen is considered to be the external surrogate for the liver motion, which is measured at 12 locations by the electromagnetic tracking system. Figure 3.11 shows the trajectories of surrogate C3 (on the left chest) and surrogate A2 (on the middle of upper abdomen). Both trajectories are of frequencies about 0.35Hz. Surrogate C3 has small amplitude in all CC, AP, and LR-directions, which is about 1.79 mm. For surrogate A2, the main movement is in the AP-direction with average amplitude 6.47 mm. The second largest movement is in the CC-direction with average amplitude 2.23 mm. And the smallest movement is in the LR-direction with average amplitude 0.78 mm.

Table 3.3 shows the average amplitudes measured from the different surrogate locations for 6 pigs. Surrogate A2 has the largest amplitude than all the other surrogates. The group of surrogates on the upper abdomen (A1 to A3) has the largest average amplitude than the others. The group of the second largest average amplitude is on the middle abdomen (A4 to A6). The surrogates on the lower abdomen (A7 to A9) have the smallest average amplitude, possibly because they are farthest from the liver. For the lower chest (C1 to C3), surrogate C2 has large movement in the AP-direction, and surrogate C1 and C3 have smaller movement due to the limitation by ribs.

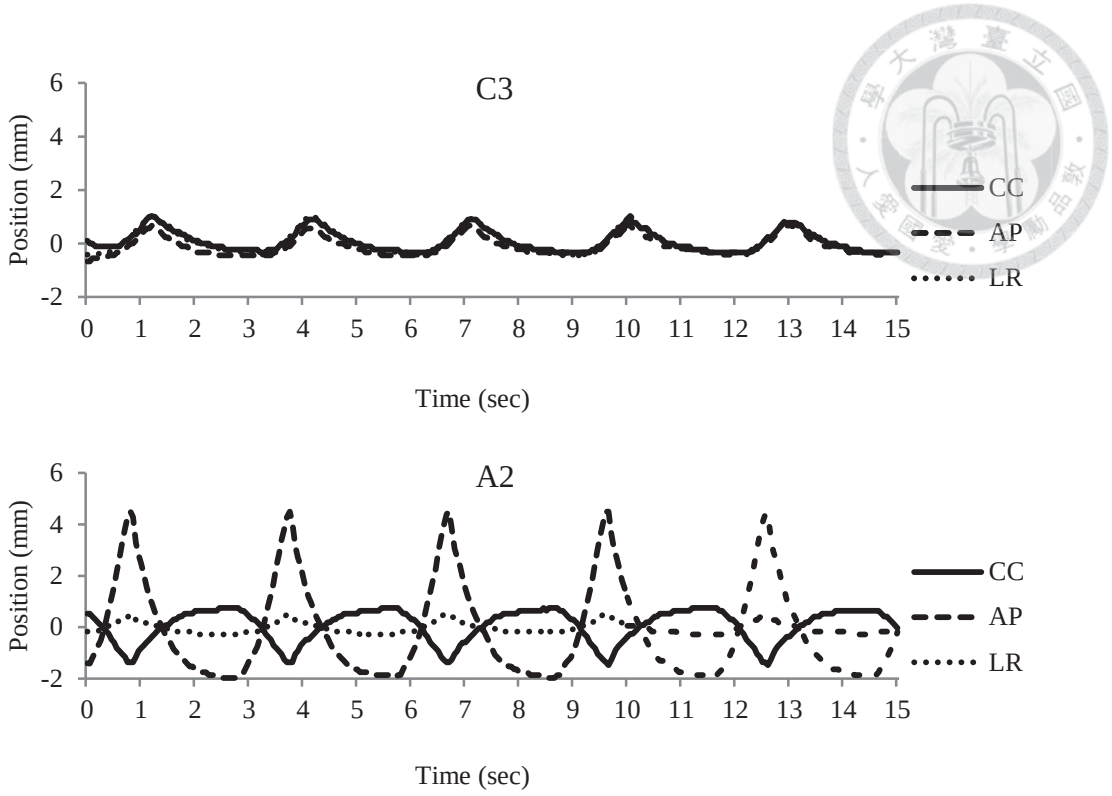

Figure 3.11 Trajectories of the external respiratory surrogates at C3 and A2. Surrogate A2 has larger movement than C3 has. Main movement is in the AP-direction, and second main movement is in the CC-direction. Movement in the LR-direction is less than in the CC and AP directions.

Table 3.3 Average amplitude and standard deviation of chest and abdominal motion for 6 pigs in the AP-direction, and the breathing frequency of each pig.

Surrogate location (mm)	Pig 1	Pig 2	Pig 3	Pig 4	Pig 5	Pig 6
C1	0.95/0.08	1.10/0.20	1.63/0.16	1.68/0.17	0.86/0.31	1.61/0.34
C2	2.97/0.18	3.93/0.55	3.56/0.18	4.50/0.44	3.06/0.12	3.58/0.49
C3	0.91/0.33	0.97/0.04	1.42/0.28	1.22/0.00	0.55/0.21	1.03/0.11
A1	4.35/0.57	5.38/1.10	5.42/0.38	5.64/0.50	2.66/0.28	5.11/0.82
A2	5.04/0.77	5.91/0.79	5.98/0.43	6.74/0.61	3.27/0.16	5.19/0.55
A3	2.54/0.68	4.75/0.61	4.96/0.52	5.09/0.61	2.67/0.22	4.37/0.71
A4	3.20/0.24	4.12/0.52	3.55/0.21	4.22/0.58	2.50/0.10	3.60/0.32
A5	3.30/0.34	4.10/0.73	4.01/0.26	4.81/0.63	3.04/0.15	3.87/0.56
A6	2.22/0.24	3.41/0.62	3.24/0.08	3.64/0.69	2.34/0.17	2.96/0.42
A7	2.49/0.17	2.73/0.34	2.21/0.45	2.30/0.71	1.78/0.12	2.57/0.68
A8	2.40/0.11	2.74/0.45	2.24/0.25	2.88/0.81	1.87/0.16	2.55/0.78
A9	2.45/0.27	2.61/0.28	2.34/0.27	3.04/0.86	1.82/0.07	2.63/0.37
Frequency (Hz)	0.39/0.01	0.34/0.06	0.33/0.02	0.34/0.00	0.34/0.00	0.34/0.00

Average/SD

■ **Liver-Abdomen Movement Correlation Development**

Linear regression, a common statistical technique for relating a dependent variable to an independent variable, helps finding a model fitting the correlation between the liver motion and the chest/abdomen motion. This model assumes that the correlation between the dependent variable *y* and the independent variable x is linear. It takes the form

$$y = ax + c \tag{4}$$

Where a and *c* are the coefficients of model. The coefficients can be calculated using the least square method [79]. The chest/abdomen wall motion and the motion of liver are measured and then analyzed. The result shows that they are highly correlated. Figure 3.12 (a) shows the linear correlation models between the abdomen motion in the AP-direction and the liver movement of IVC in the CC, AP, and LR directions, and Figure 3.12 (b) shows the distribution of the modeling error in each direction.

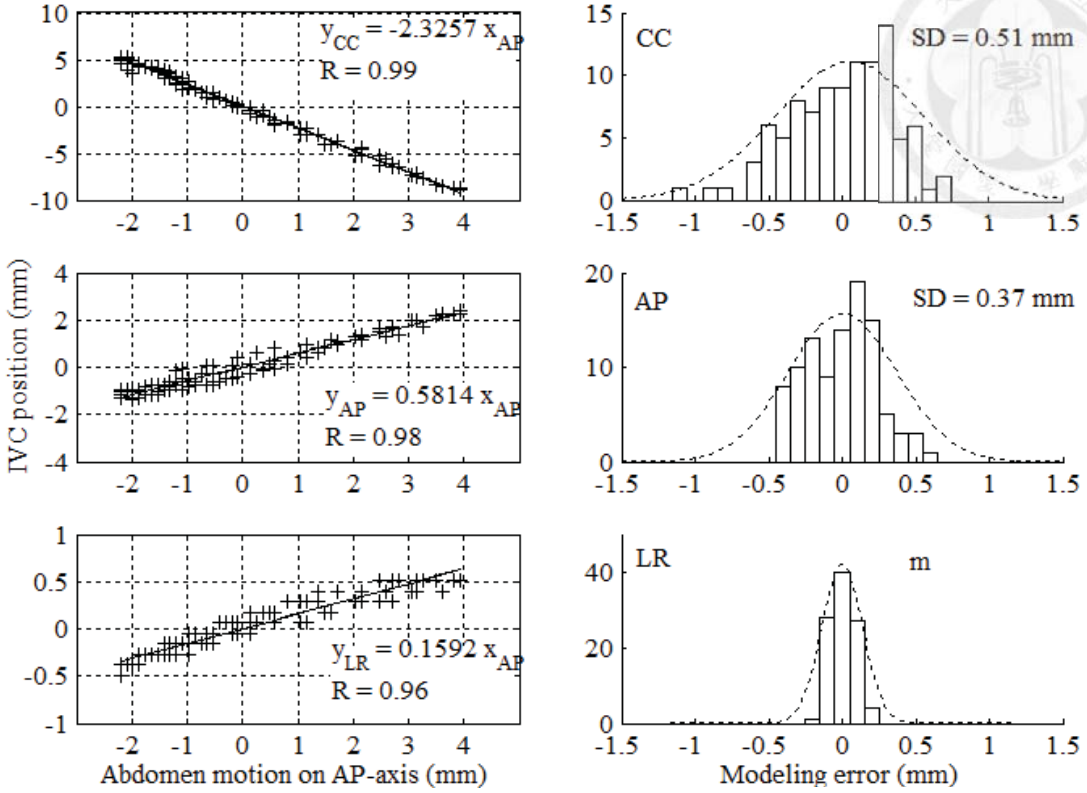

Figure 3.12 Results of correction modelling. (a) Correlation models (linear models) between the abdomen motion on the AP-axis and the liver movement of IVC on the CC, AP, and LR-axes. (b) The bar charts of the modeling errors in three axes.

3.3.4 Estimation Results and Discussions

This section shows the estimation results using single external surrogate from different locations, discusses the benefits of multi-surrogate signals, and shows the validity of a 10-minute long-term estimation results.

■ **Signal Surrogate Modelling Error**

This section discusses the ideal location for surrogate by analyzing the estimation accuracy. The liver motion estimation in this study is split model-fitting and motion estimation. The first 15 seconds of the surrogate signals and the liver motion signals are used to construct a linear-correlation model in the first stage. The model can then be used to estimate the liver motion with the external surrogates. The estimation error is defined to be the difference between the estimated liver motion and the measured liver motion.

Figure 3.13 shows average estimation errors of IVC, TRL, and TLL using different surrogates for 3 pigs. The estimation errors with all the surrogates are less than 1.5 mm. Among all the surrogates, surrogate A2 achieves the smallest estimation error, meaning that A2 has the best estimation accuracy and shows the best location for a surrogated sensor. Moreover, surrogate C2, A1, and, A3 also have quite small estimation errors to be good locations for surrogate sensors. Surrogate A7 to A9 have the largest estimation errors, possibly because they are far from liver. The area should be avoided in liver motion estimation.

Compared with the absolute estimation errors, TRL and TLL have smaller errors than IVC. However, the percentage errors of surrogate A2 are similar for TRL, TLL, and IVC as well. The average amplitude of IVC is 11.98 mm and its estimation error is

0.6 mm, which corresponds to a percentage error of 5.01%. While TRL has the average amplitude 7.36 mm, the estimation error 0.42 mm, and the percentage error 5.7%. TLL has the average amplitude 7.77 mm, the estimation error 0.4 mm, and the percentage error 5.1%. Therefore, estimation performances of IVC, TRL, and TLL are similar, although their average amplitudes are different.

To summarize, the middle of upper abdomen (A2) is the best location for surrogate signals measurement. Moreover, the upper abdomen (A1 to A3) and the xiphoid process (C2) are also good locations for external respiratory surrogates.

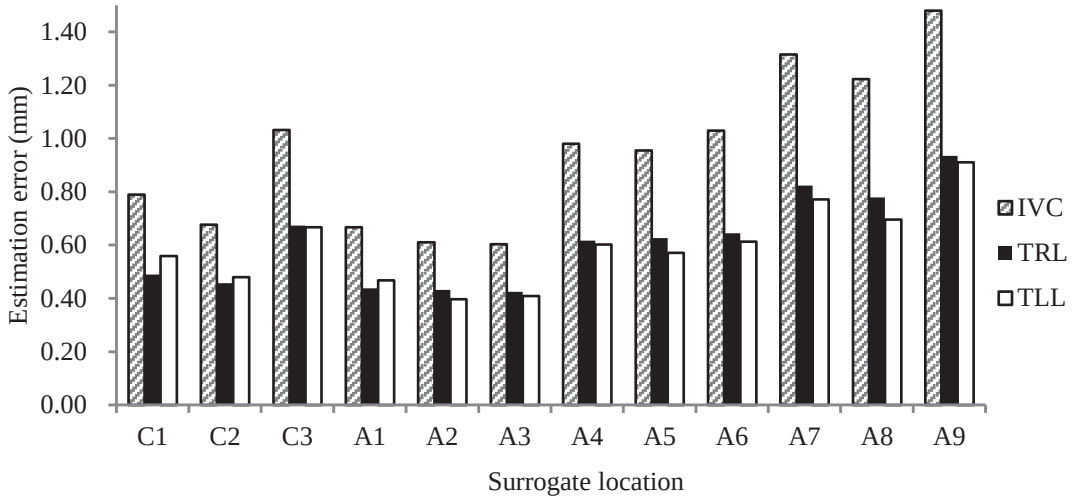

Figure 3.13 Estimation errors using different external respiratory surrogates for 3 pigs. Estimation errors of IVC are larger than TRL and TLL. Surrogate A2 has the best estimation accuracy. Surrogate A1, A2, and A3 (the upper abdomen) have better estimation accuracy, and surrogate A7, A8, and A9 (the lower abdomen) have worse estimation accuracy.

■ **Multi-Surrogate Modelling Error**

This section compares estimation performances of multi-surrogate models with the single-surrogate models. The single-surrogate models use only one surrogate to fit the correlation and the estimation results are shown in the previous section. From the results, surrogate A2 is shown to have the best estimation accuracy. Surrogate C2 is the anatomic landmark with good estimation accuracy as well. Therefore, C2 and A2 are selected to combine with other surrogates to test the validity of the multi-surrogate model for liver motion estimations. Figure 3.14 shows the estimation results of IVC, TRL, and TLL using multi-surrogate and single-surrogate models for 3 pigs. The first ten estimation errors are from the results of the multi-surrogate models, while the last twelve errors are from the results of the single-surrogate models.

As we can see, all estimation errors from multi-surrogate models are less than 0.5 mm. In general, TRL and TLL have better estimation accuracy than IVC. For IVC, all multi-surrogate models have better estimation accuracy than the single-surrogate models, with the only exception of the result from the C2/A2/A8 model. Similarly for TRL, only C2/A2/A6 model has larger estimation error than the single-surrogate model. For TLL, only C2/A2/A9 model has larger estimation error than the single-surrogate model. According to the results from the single-surrogate models, the models which have a surrogate located on the middle or lower abdomen have worse estimation.

Although these models produce larger estimation error than the best result produced by single-surrogate models, the differences of them are less than 0.05 mm. Therefore, the overall multi-surrogate method produces better estimation than the single-surrogate method.

Overall results shows that the chest (C1 to C3) and upper abdomen (A1 to A3) have better multi-surrogate estimation accuracies than the single-surrogate models such that they are good locations for multiple surrogates. In conclusion, the multi-surrogate models can improve the estimation accuracy of liver motions with most errors less than 0.4 mm.

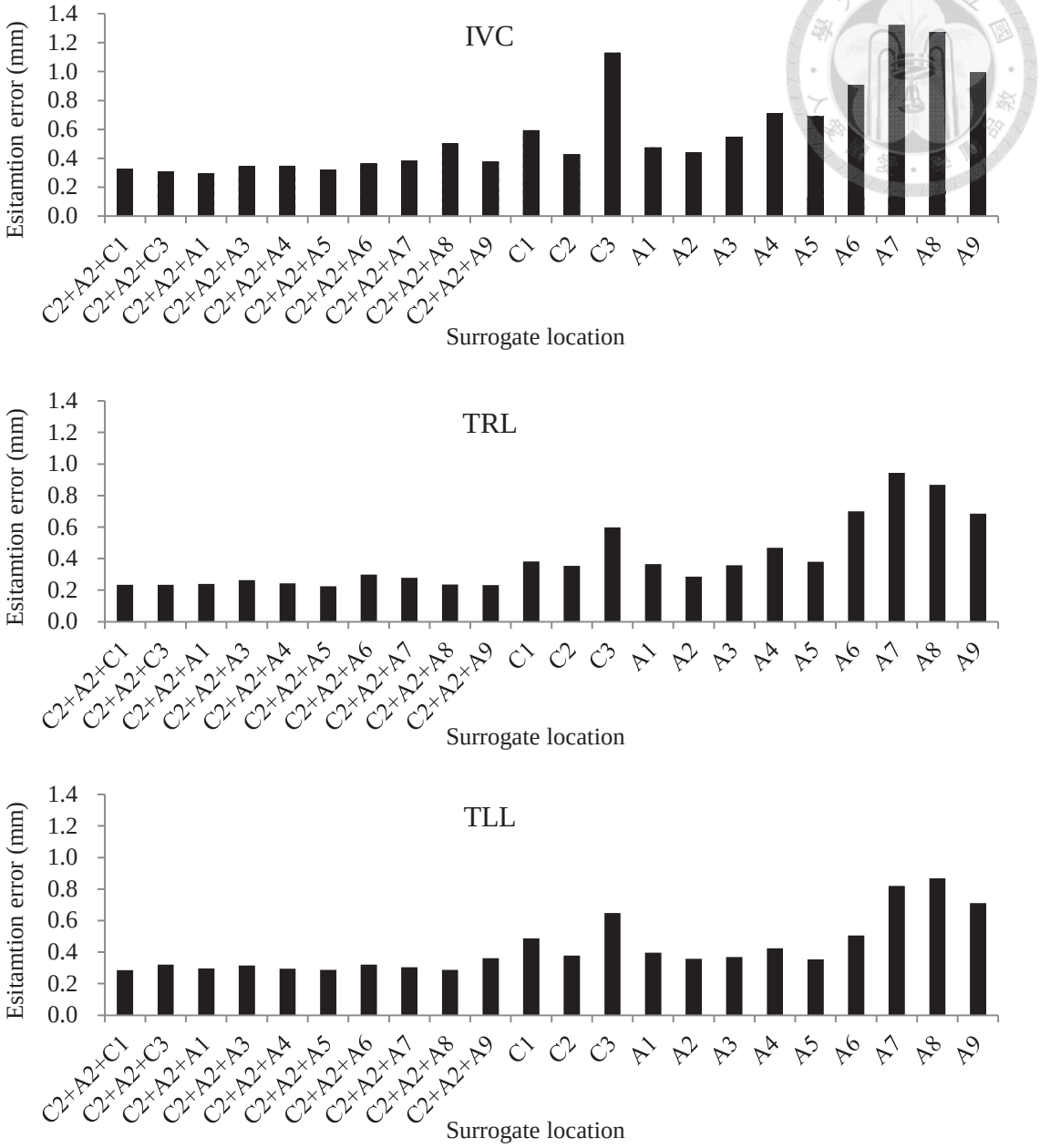

Figure 3.14 Estimation errors of IVC, TRL, and TLL using multi-surrogate and single-surrogate for 3 pigs. Excluding the C2/A2/A8 model at IVC, the models with multi-surrogate have better estimation accuracy than single-surrogate models. Estimation errors from the multi-surrogate are less than 0.4mm.

■ **Long-Term Modelling Error**

In this section, long-term surrogate signals for the period of ten minutes are used to demonstrate the reliability of correlation model for long-term estimation. Signals from the first 15 seconds provide a baseline correlation model, and then the model is used to estimate liver motion for the remaining period of time. Figure 3.15 shows the long-term liver motion estimation errors for 3 pigs (pig 4, 5, and 6).

For pig 4 and pig 6, the estimation error stably remains within 0.9 mm for the entire 10 minutes. For pig 5, the estimation error is stable for the first 6 minutes, and then they rise slightly from 0.5 mm to 1.4 mm between 6 and 7 minute. After that, the error decreases slowly to under 0.8 mm. In the case of pig 5, the estimation errors have variations between 0.5 mm to 1.5 mm during the 10 minutes. According to Figure 9, the changes of liver motion boundaries are limited in the range of 1 mm during the 10 minutes. It means that the liver motion is constrained since the respiration motion. Therefore, the estimation error would be stable in a limited boundary for long-term. The error variation of extended duration will be studied in the future.

Overall, the estimation errors are considered to be stable for the period of 10 minutes with errors less than 1.4 mm. Therefore, the linear-correlation models are reliable in estimating long-term liver motions.

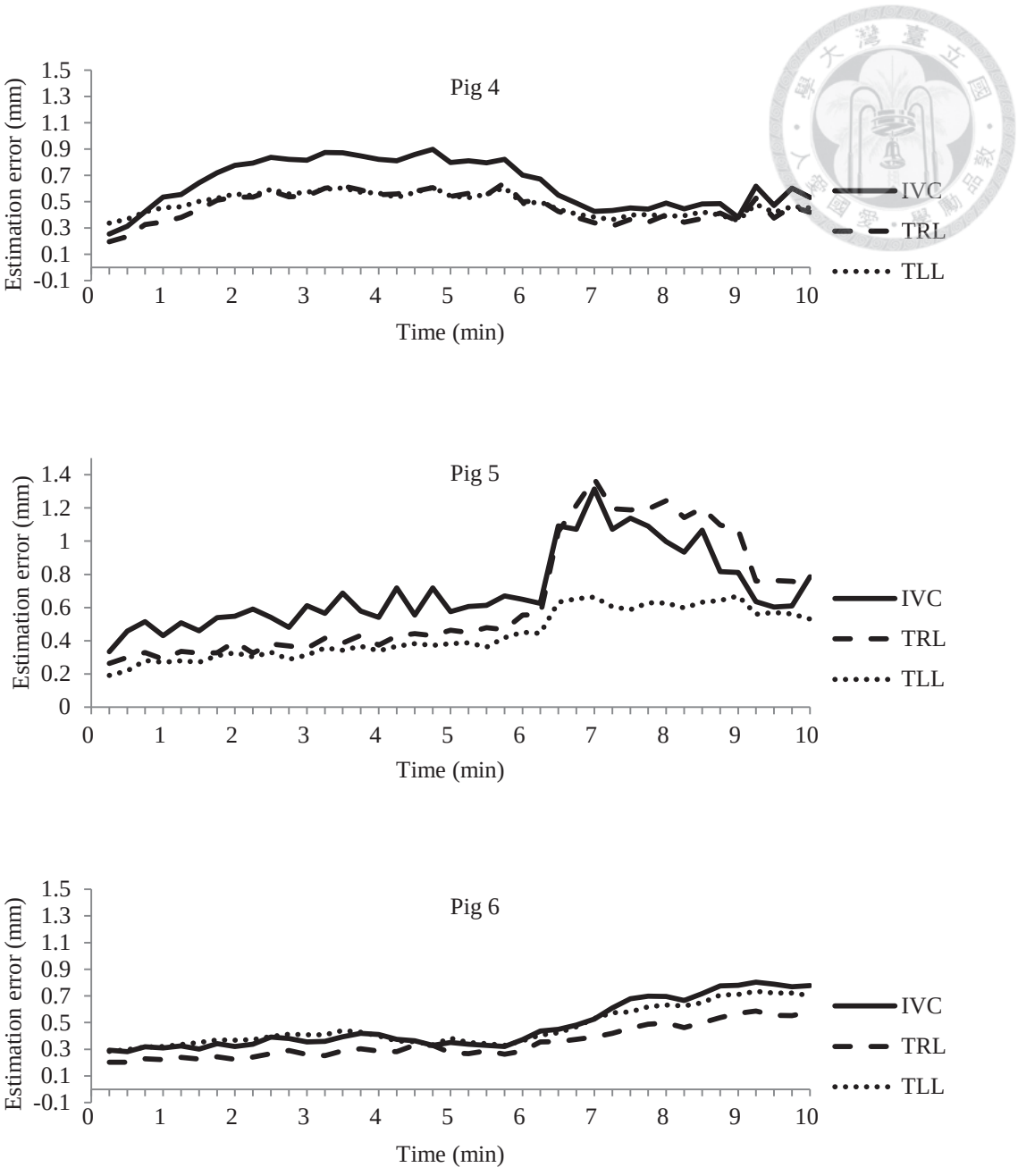

Figure 3.15 Long-term estimation error of IVC, TRL, and TLL using surrogate A2 for 3 pigs. Correlation model is built using the first 15 seconds of signals, estimating liver motion in continuous time. Estimation error is less than1.4 mm in 10 min.

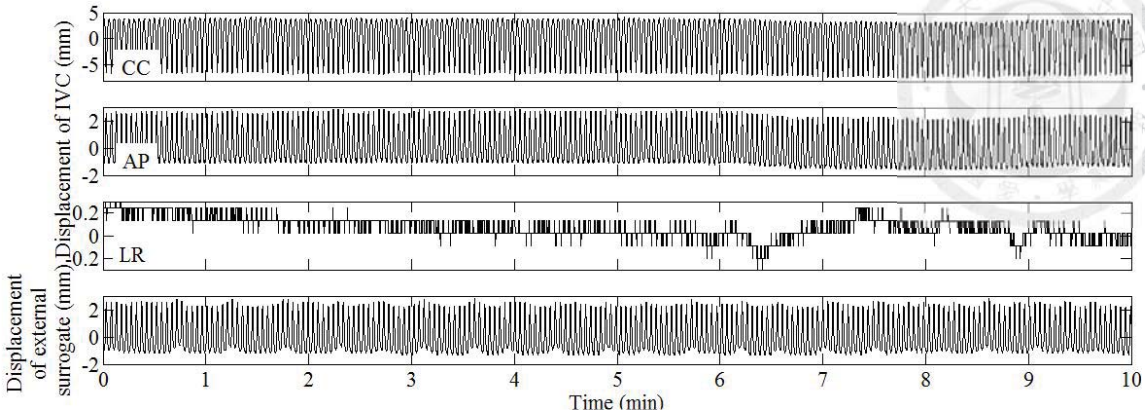

Figure 3.16 The raw data of liver (IVC) motion and external surrogate signals in 10 minutes. The largest movement of liver is on the CC-axis, and the less movement of liver is on the LR-axis. The motions of the liver and the surrogate are stable with small vibration which is less than 1 mm.

The aim of this chapter is to establish a liver motion estimation method based on external respiratory surrogate signals to guide treatment devices. In this study, external respiratory surrogates from chest/abdomen motions are used to estimate the liver motion accurately. The single-surrogate and multi-surrogate models are constructed to identify the best area for surrogate arrangement and to analysis the possible benefit of using multiple surrogates. The reliability of models is also verified in 10 minutes experiment. The results show that the best location for surrogate arrangement is around the middle of upper abdomen (surrogate A2), while multiple surrogates do bring benefit for liver motion estimation. The estimation error is reduced from 0.6 mm in single-surrogate cases to 0.4 mm in multi-surrogate cases. Moreover, the data also show that the estimation model can maintain its accuracy with 1.4 mm, which is quite acceptable in

normal treatment, for long-term period of 10 minutes. However, the long-term estimation errors increase slightly. It seems there are distributions in external signals and established models. To reduce the estimation error induced by the time, a model updating mechanism is essential and will be studied in the future.

For single-surrogate cases, the models established by the surrogates located on the upper abdomen (surrogate A1 to A3) have better estimation results than others, and the middle of upper abdomen (surrogate A2) has the best estimation result (Figure 6). It is possible that they are much closer to the liver than others, so their movements have stronger correlation with liver's movement. Moreover, the amplitudes of these locations are larger than others (Table II), so they could provide good related signals for estimation model establishment. For the human cases, the candidate location for external surrogate arrangement could be selected through these criteria: being close to the liver and with larger motion amplitude.

From the results of multi-surrogate cases, all multi-surrogate models produce better estimation performance, and estimation errors are less than 0.4 mm. Multiple surrogates enhance estimation accuracy for liver motion. Combining the results from single-surrogate and multi-surrogate cases, the locations for external surrogate arrangement could be selected on the area near the target, such as a liver tumor, and multi-surrogates could be used to improve the accuracy.

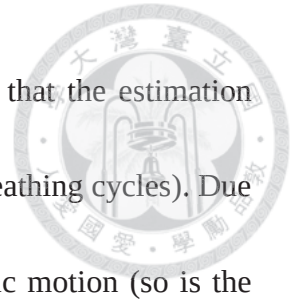

For long-term estimation cases, our preliminary studies show that the estimation error is between 0.5 mm to 1.5 mm within 10 minutes (about 150 breathing cycles). Due to the fact that the respiration motion is a constrained semi-periodic motion (so is the induced liver motion), we do not expect the modeling error to diverge with time. Part of the errors may be induced by the disturbances to the external surrogate signals, which should also be bounded. Further studies will be performed for time durations from 30 minutes to 120 minutes. The possibly bounded, but semi-periodic error behavior will be studied in the future. Moreover, model updating algorithm will be added if it is necessary to keep the error within a reasonably small bound.

3.4 Summary

In summary, CT-to-physical registration using external markers provides liver tumor positons to build correlation model, and external respiratory surrogate signals perform good estimation results to obtain liver movement. This chapter has established a liver motion estimation method based on external respiratory surrogate signals involving an end-points registration for liver tumor tracking. It has potential to apply into clinical liver tumor tracking.

Chapter 4 Tracked Ultrasound with CT Image Registration

In this chapter, a novel liver tumor tracking by tracked ultrasound involving CT image is proposed. The concept of this approach is to track liver tumor position by tracking the liver position, and it is shown in Section 4.1. In Section 4.2, a real-time tracking phantom experiment is conducted. The experiment results and approach performance are shown in Section 4.3. Discussions and a summary are in Section 4.4.

4.1 Proposed Approach

The overall concept of the proposed method is to locate the liver tumor position by determining the tumor position inside the liver and locating the liver position. Since CT scan is able to obtain the anatomical structure of the liver, the tumor position inside the liver could be determined. In order to locate the liver position, tracked ultrasound is used to detect the position of the cross section of the liver. Since liver has various cross-sectional views due to its uniform shape, the relationship between the cross section and the liver can be obtained by matching the cross section from the ultrasound and the liver shape from the CT, called ultrasound/CT image registration. The liver position can be acquired by combining the information of the liver cross section

position from the tracked ultrasound and the relationship between the cross section and the liver. Adding the information of the tumor location in the liver from the CT, the tumor location can be estimated by coordinate transformation.

The proposed method consists of preoperative and intraoperative stages. In the preoperative stage, the patient is scanned by CT. The liver is constructed into a 3D model, and the tumor location relative to the liver is then determined. In the intraoperative stage, the surgeon scans the patient's abdomen to detect the location of the liver by tracked ultrasound. The liver location is acquired via tracked ultrasound and image registration. At last, the tumor location is transformed from the liver into the world coordinate. To be specific, tumor location can be mapped from the liver coordinate into the world coordinate through the following transformation:

$$^{World}q = {}^{World}T_{US}\ {}^{US}T_{Liver}\ {}^{Liver}q \tag{5}$$

where ${}^{A}q$ stands for the object position relative to the *A* coordinate. ${}^{B}T_{A}$ is the transformation from the *A* coordinate to the *B* coordinate, and it is reversible. Each point in the *A* coordinate, ${}^{A}q$, can be transferred from the *A* coordinate into the *B* coordinate; its position in the *B* coordinate is noted as ${}^{B}q = {}^{B}T_{A}\ {}^{A}q$. Figure 4.1 shows the relationship between each set of coordinates. The tumor location can be translated from the liver coordinate into the world coordinate via measuring the relationship between

coordinates. This is the central concept of the proposed tracking method.

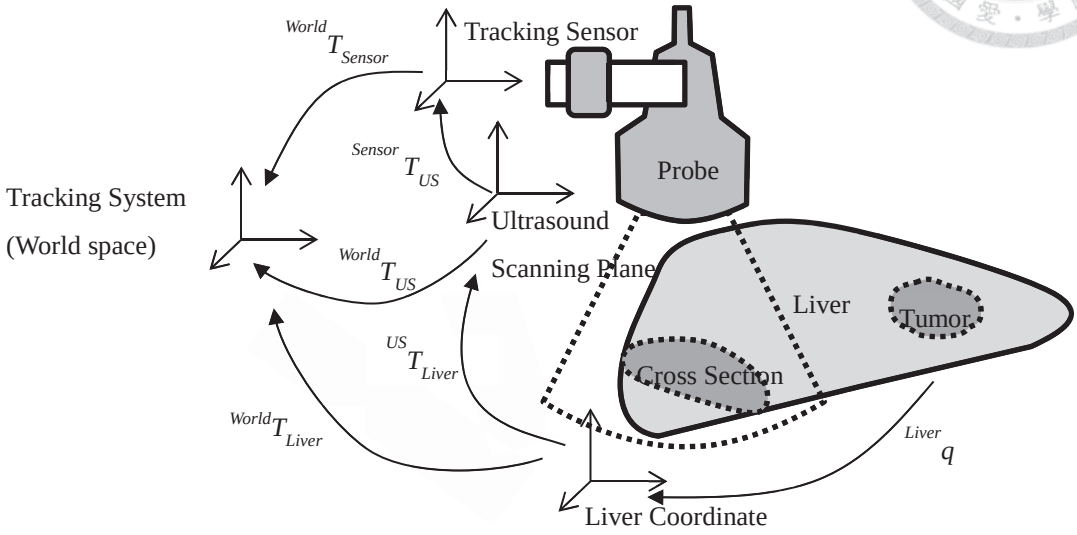

Figure 4.1 Illustration of tracking of liver tumors by transferring the tumor location from liver coordinate into the world coordinate. The tumor location in the liver is measured from preoperative CT scan while the liver position is acquired by intraoperative tracked ultrasound.

As is generally known, the liver is not a rigid organ so it might get deformed due to the pressure from the diaphragm while breathing [17, 19, 20, 80]. The pressure might affect the accuracy of the tracking because the shape and the size of liver may change. According to the liver motion data from an *in vivo* animal experiment in Chapter 3, the deformation of the liver induced by respiration is relatively small and it can be ignored because all variations of distance between three landmarks of liver (the inferior vena cava, the lower tip of right hepatic lobe, and the lower tip of left hepatic lobe) are less

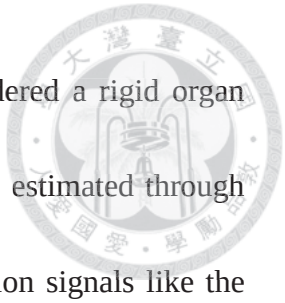

than 1.3% [80] (shown in appendix). Therefore, the liver is considered a rigid organ while breathing in this study. However, the live deformation can be estimated through the relationship between the liver motion and other related respiration signals like the movement of diaphragm [35, 70, 74, 81] and abdominal wall [42, 73, 74], so it can be compensated for accordingly.

4.1.1 Computed Tomography

Computed tomography (CT), a preoperative medical image technique, is used to provide the information of the liver shape for ultrasound-CT image registration and the tumor location inside the liver for position transformation. Once the CT spatial positions of the liver and the tumor are obtained, the position of the tumor inside the liver can be computed. The used CT scanner, Toshiba Activion 16 (Toshiba Medical Systems Corporation, Tokyo, Japan), features 16 detectors with 0.5 mm width and 0.75 sec scanning time, so it can scan the area of approximate 10 mm per second. The field of view is around 350 mm, and the resolution in scanning plane is 512 $\times$ 512 pixels. The thickness and interval of the CT slice are 3 mm and 1 mm, respectively.

In this study, the shape of the liver is used as a feature for image registration. It is obtained by watershed segmentation as the liver is very prominent due to the intensity in the CT image. It can segment the liver and other tissues based on the texture and the

intensity information [82] (as shown in Figure 4.2). The detected liver shape is used as the database for image registration. The area of the detected liver images is also calculated as the minor feature for registration. Tumors are distinguishable in CT, and they are also segmented by watershed.

(a) (b) (c)

Figure 4.2 Liver segmentation from CT image. (a) CT image including the liver, agar, sensor, and the air in the vessel. (b) Segmented image of the liver from CT image. (c) Contour of the liver from CT image.

In order to determine the relationship between the CT and the ultrasound, tracked ultrasound and the CT image should be transferred to the same coordinate which is the tracking system coordinate (referred to as the world coordinate in this study). The transformation from the CT to ultrasound scanning plane is ${}^{US}T_{CT} = \left({}^{World}T_{US}\right)^{-1}\,{}^{World}T_{CT}$, where $\left({}^{World}T_{US}\right)^{-1}$the inverse form of ${}^{World}T_{US}$, which is obtained from reading the position of the sensors attached to the tracked ultrasound. ${}^{World}T_{CT}$ is the transformation from the CT to the world coordination and it can be obtained by calculating the relationship of the markers or sensors in the two sets of coordinates by a transformation method known as CT-to-physical registration.

4.1.2 Tracked Ultrasound

Tracked ultrasound is a technique to locate the object scanned by ultrasound probe via attached tracking sensors. The sensors are fixed on the ultrasound probe to measure the location of the probe in the tracking system coordinate. The position of the object displayed in the ultrasound image is then transferred into the world coordinate as shown in Figure 4.1. The object's position can be obtained via coordinate transformation:

$$^{World}q = {}^{World}T_{Sensor}\ {}^{Sensor}T_{US}\ {}^{US}q \tag{6}$$

where ${}^{Sensor}T_{US}$ is fixed, measured by calibration, and ${}^{World}T_{Sensor}$ is variable, measured by reading the position of the sensors relative to the tracking system (world coordinate) [83, 84]. The transformation from the ultrasound scanning plane to the world coordinate is

$$^{World}T_{US} = {}^{World}T_{Sensor}\ {}^{Sensor}T_{US} \tag{7}$$

Since 1998, tracked ultrasound has been studied for 3D model reconstruction and spatial tracking. There are two methods to track the location of the ultrasound probe: optical and electromagnetic tracking. Optical-tracked ultrasound is attached visible markers. Carbajal *et al.* presented an optical-tracked ultrasound with 2.0 ± 1.6 mm tracking error using abdominal ultrasound probe [85]. Electromagnetic-tracked ultrasound (EM-tracked ultrasound) uses electromagnetic sensor to measure the position and

orientation of the ultrasound probe. Zhang *et al.* proposed a 2.5 ± 0.6 mm tracking error EM-tracked ultrasound with [86]. Melver *et al.* presented an EM-tracked ultrasound with 3.4 ± 2.3 mm tracking error at 14 cm depth [87].

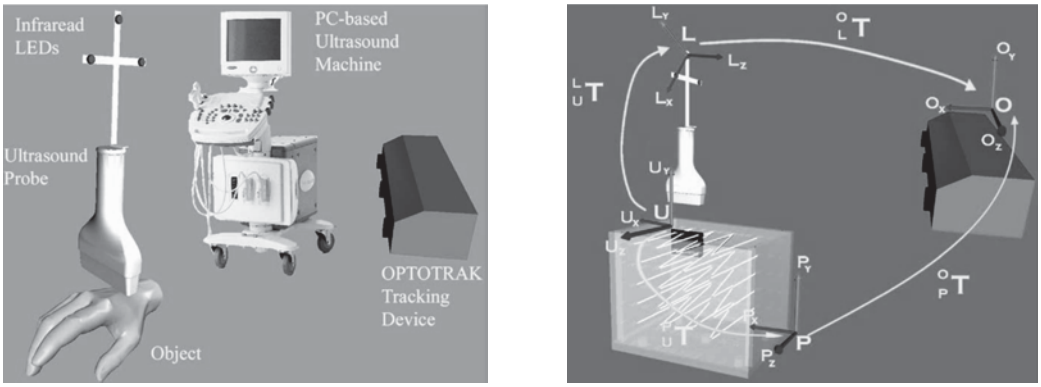

(a) (b)

Figure 4.3 Illustration of tracked ultrasound [66]. (a) Optical tracked ultrasound consists of an ultrasound device and an optical tracking device. (b) Illustration of coordinate transformation from ultrasound image to an optical tracking system.

In this study, the tracked ultrasound consisting of a diagnostic ultrasound device and a 3D tracking system was used in this study. The ultrasound device, ALOKA SSD-500 (Hitachi Aloka Medical, Ltd., Tokyo, Japan), features a 3.5 MHz convex probe and displays B-mode images in real time. The scanning plane is a fan shape with a 60 degree scanning angle and a 17 cm depth. The tracking system is a real-time electromagnetic tracking system, 3D Guidance trakSTAR (Ascension Technology Corporation, Burlington, VT), that features a magnetic field generator with $46 \times 56 \times 60$ cm working space and four columnar sensors with 10 mm length and 2 mm diameter. The sampling rate of tracking system is 20 Hz and the resolution is 0.1 mm.

4.1.3 Ultrasound-CT Image Registration

The organs in the abdomen can be mapped from the CT coordinate into the world coordinate via CT registration. With this method, however, the liver location cannot be absolutely ascertained as it is moving in the abdomen while breathing. To detect the actual liver location, registration is essential. Medical image (ultrasound, CT, and MRI) registration has been presented since 2000 [88]. It includes 2D to 3D and 3D to 3D image registration. Penney *et al.* proposed an anatomic-landmark-based registration method based on liver vessel information and the registration error was between 2.7 to 3.5 mm [67]. Leroy *et al.* reported an intensity-based registration method for kidneys in 2004. The registration error was 7.7 ± 3.5 mm, and it took around 80 sec (from 11 to 170 sec) [89, 90]. In 2013, Xu *et al.* presented an ultrasound effect simulation form CT image to register the ultrasound image. The fiducial and target registration errors were 3.81 ± 1.16 mm and 4,13 ± 1,27 mm with averagely 76 sec acquisition time [91].

One of the important issues is that the run time of 3D image registration is too long (over 60 sec), and it is inadequate for real-time tracking. For real-time tracking, 2D to 2D image matching is used as it requires less computing time than 3D matching. However, it is difficult to choose the candidate plane for image matching. An alignment approach is added in front of the registration to make the ultrasound scanning plane parallel to the CT slices. After the alignment, the ultrasound image is matched to the CT

slices in-plane and along the slice-direction to determine the relationship between the ultrasound and the liver (as shown in Figure 4.4).

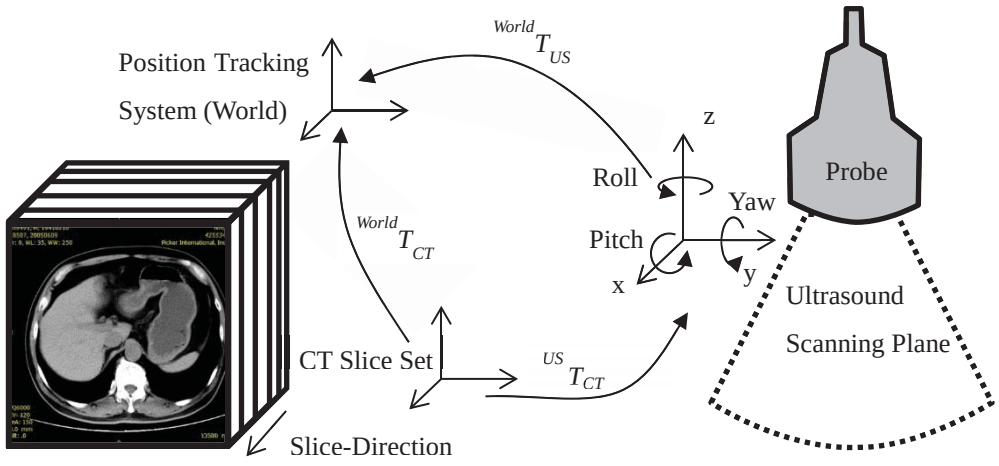

Figure 4.4 The relationship between the ultrasound scanning plane and CT slice set can be obtained by transformation of the ultrasound and CT that are relative to the same coordinate (world coordinate).

The registration consists of alignment and 2D image matching. In alignment, the ultrasound scanning plane is adjusted parallel to the CT slices, so the relative angles between them are equal to 0. In other words, the value of the orientation parameters (yaw, pitch, and roll) in the transformation equals to 0. Here, we assume that the liver and its CT 3D model have the same coordinate, ${}^{US}T_{Liver} = {}^{US}T_{CT}$. The transformation from ultrasound to CT can be then calculated as ${}^{US}T_{CT} = \left({}^{World}T_{US}\right)^{-1} {}^{World}T_{CT}$, as shown in Figure 4.4. It can be also expressed in the following form indicating

translation parameters (x, y, and z) and orientation parameters (yaw, pitch, and roll):

$$
{}^{US}T_{CT}
$$

$$
= \begin{bmatrix} C(\gamma)C(\beta) & C(\gamma)S(\beta)S(\alpha) - S(\gamma)C(\alpha) & C(\gamma)S(\beta)C(\alpha) + S(\gamma)S(\alpha) & x \\ S(\gamma)C(\beta) & S(\gamma)S(\beta)S(\alpha) + C(\gamma)C(\alpha) & S(\gamma)S(\beta)C(\alpha) - C(\gamma)S(\alpha) & y \\ -S(\beta) & C(\beta)S(\alpha) & C(\beta)C(\alpha) & z \\ 0 & 0 & 0 & 1 \end{bmatrix} \quad (8)
$$

where α stands for yaw, β stands for pitch, and γ stands for roll. $S(a)$ is noted as $sin(a)$, and $C(a)$ is noted as $cos(a)$. The values of yaw, pitch, and roll can be calculated from the transformation. The ultrasound probe is adjusted to make all orientation parameters equal to 0. After alignment, the ultrasound probe is fixed to detect the liver position continuously by image matching.

In image matching, 2D cross-correlation (2D XCC), a common image matching approach to measure the similarity of the two images, is used to find the correlation between the liver images from the CT and the ultrasound. It detects the correlation coefficient relative to the template (liver image from the ultrasound) in a larger image (liver image from the CT). The position with the highest coefficient is the location most similar to the template in the whole image [92]. The formula of 2D cross-correlation coefficient is written as

$$
C(u,v) = \frac{\sum_{x,y}\left(A_{x,y} - \bar{A}_{x,y}\right)\left(B_{x,y} - \bar{B}_{x,y}\right)}{\sqrt{\sum_{x,y}\left(A_{x,y} - \bar{A}_{x,y}\right)^2 \sum_{x,y}\left(B_{x,y} - \bar{B}_{x,y}\right)^2}} \quad (9)
$$

where A stands for the image, and B stands for the template. $A_{x,y} = A(u + x, v + y)$ stands for the local image at location (u, v) with $x \times y$ size, and $\bar{A}_{x,y}$ stands for the mean of the image underneath the temple size at location (u, v). $B_{x,y}$ stands for the template with $x \times y$ size, and $\bar{B}_{x,y}$ stands for the mean of the template. The range of the coefficient is from -1 to 1. The image is directly correlated to the template if the correlation is positive; the image is inversely correlated (anti-correlated) to the template if the correlation is negative. The absolute value of the coefficient that is between 0.7 and 1 can be considered highly correlated. It is moderately correlated while it is in the range from 0.3 to 0.7, and it is considered as low-correlated while it is less than 0.3.

In image registration, the image of the liver segmented from the CT stands for the input image, and the liver image from the ultrasound serves as the template, as shown in Figure 4.5 (a) and (b). The magnitude of correlation after correlation calculation is shown in Figure 4.5 (c). The position with the highest coefficient is the place that most resembles the template. The area which is most similar is obtained (Figure 4.5 (d)). The translation parameters on the slice plane (*x* and *y*) are obtained. The ultrasound template matches with the CT images along the slice direction. The slice which has the highest coefficient is the place the ultrasound scanning plane located, and the translation parameter along the slice direction, *z*, is obtained.

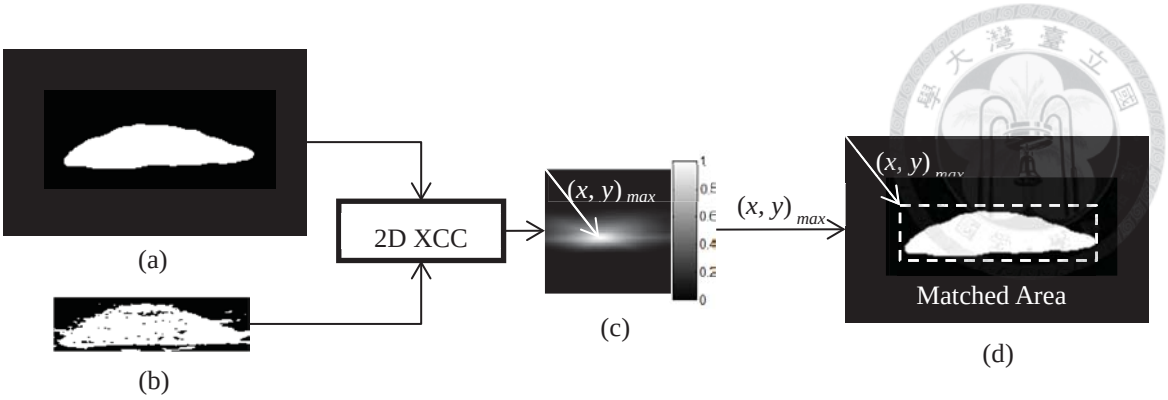

Figure 4.5 An example of a 2D cross-correlation: (a) the image of the liver segmented from the CT, (b) the image of the liver from the ultrasound image used as a template, (c) the magnitude of the correlation coefficient, (d) the matched area in the CT. The point $(x, y)_{max}$ with the highest value in the coefficient plane is the best matching area.

4.2 Experiment Design

Two experiments including static localization and real-time tracking are conducted using pig liver phantom to verify the tracking performance of the proposed approach.

■ Phantom for Experiment

The shape of the liver is unique, so it can be used as a feature for image registration. In the CT image, liver has different intensity than other tissues in gray scale, and it is displayed in gray. Moreover, the fat is displayed in dark shades whereas bones are displayed in white (Figure 4.6 (a)). In the ultrasound image, the liver has a special pattern and intensity because of its property of echo-reflection. The surface of the liver is obvious due to the high echo reflectivity at surface, as shown in Figure 4.6 (b). In

order to verify the performance of the proposed method, a phantom is made for the experiments. The image property of the phantom in the CT and the ultrasound should be similar to the human liver.

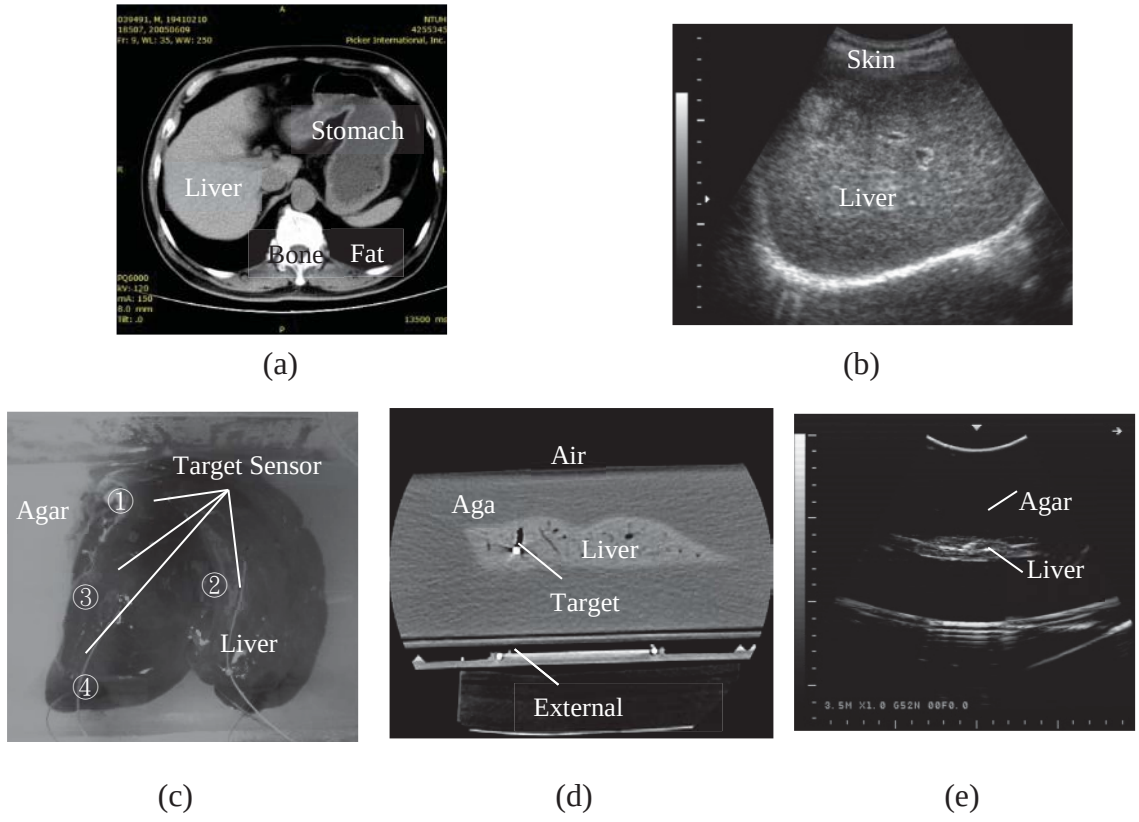

(a) (b)

(c) (d) (e)

Figure 4.6 (a) The CT image of a human abdomen, (b) the ultrasound image of a human liver, (c) phantom which consists of a pig liver fixed by agar with the arrangement of the reference sensors, (d) the CT image of the liver with agar and the sensors, and (e) the ultrasound image of the liver and agar.

The phantom which consists of a pig liver fixed in a tank filled with agar and four tracking sensors that serve as references was used in this study, as shown in Figure 4.6 (c). In the CT image, the phantom is displayed in varied intensity due to the difference in their x-ray absorption (Figure 4.6 (d)). Tracking sensors have highest absorption, so

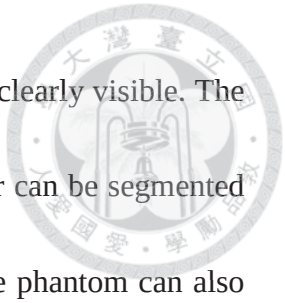

they appear as white in the CT image. The position of the sensors is clearly visible. The pig liver and agar are displayed in different shades of gray. The liver can be segmented based on the color intensity. In the ultrasound image, the liver in the phantom can also be distinguished due to its high echo-reflectivity, especially at the surface between the liver and agar (Figure 4.6 (e)). The agar has uniform texture and less echo-reflective, so its area appears dark. The intensity differences between the liver and agar are features for liver segmentation. The divided images of liver from CT and ultrasound will be used in image registration to develop the relationship of CT and ultrasound images.

- **Experiment Setting**

In the experiments, to establish the liver position using tracked ultrasound and preoperative CT, a pig liver is placed in an agar-filled tank, and a tracked ultrasound system is fixed above the tank with a three degree-of-freedoms (DOFs) mechanism for CT to ultrasound alignment (in Figure 4.7). The tank is put on a base and driven by a controlled servo motor to simulate the liver motion. The base is still and attached three tracking sensors for CT registration to simulate the external sensors attached to the patient's back. Moreover, four tracking sensors are attached to the liver to stand for the tumors and the references. The position of the reference sensors are obtained by reading the measurement from the position tracking system and are only used for verification.

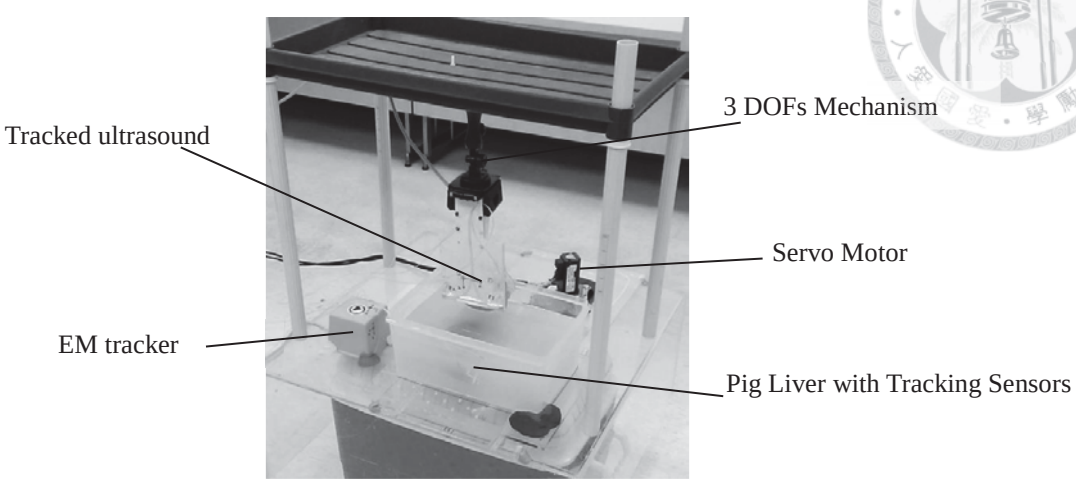

Figure 4.7 Experiment setting to simulate real-time tracking.

■ **Experiment Procedure**

There are two main stages in the experiment: (1) preoperative CT scan to detect the tumor location in the liver and to obtain liver image, and (2) the tumor tracking using intraoperative tracked ultrasound with CT to ultrasound image registration.

The preoperative stage consists of three steps:

1. Liver and tumor image acquisition via CT scan
2. Liver image segmentation
3. Tumor location computation

The liver images segmented from the CT are used as the database for image registration, and the tumor location relative to the liver is used to transform the tumor location from the liver into the world coordinate.

In the intraoperative stage, a six step procedure is followed to estimate the tumor location (as shown in Figure 4.8).

1. Tracked ultrasound alignment (initialization)
2. Liver image segmentation from ultrasound images
3. Transformation from the CT to the ultrasound acquisition by CT to ultrasound image registration
4. Transformation from the ultrasound to the world coordinate acquisition
5. Tumor tracking via coordinate transformation
6. Reference sensors' position measurement by the tracking system (for verification only)

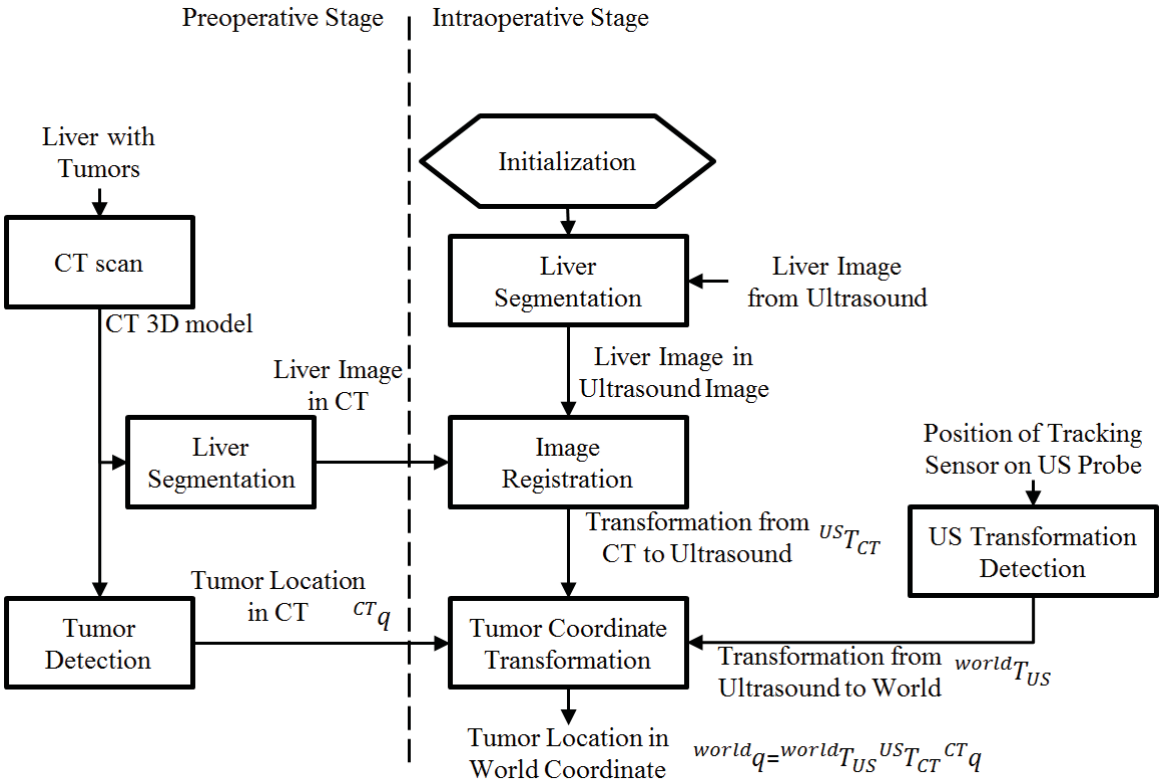

Figure 4.8 Flow chart of the proposed tracked ultrasound tracking.

In order to verify the proposed method, two experiments were conducted: static localization and real-time tracking. In the static localization experiment, the phantom with reference sensors was static. In the real-time tracking experiment, the phantom and the sensors followed a set of trajectory. The motion was a wave with a 30 mm amplitude and a 6 sec period, similar to human respiration, while the motion occurred in the cranial-caudal direction.

4.3 Experiment Results

Results of experiment are shown in this section, including static localization and real-time tracking.

4.3.1 Static Localization

Three pig livers were used to verify the proposed approach. Four position sensors were attached to each liver for reference. The experiment was repeated five times for the purpose of data collection. The static localization error as the difference between the located position and the reference position was established as 3.8 ± 1.6 mm (mean ± STD) for $N = 60$ (4.3 ± 1.6 mm in case 1, 3.7 ± 1.3 mm in case 2, and 3.6 ± 1.1 mm in case 3) with values ranging from 0.69 to 8.5 mm, as shown in Figure 4.9.

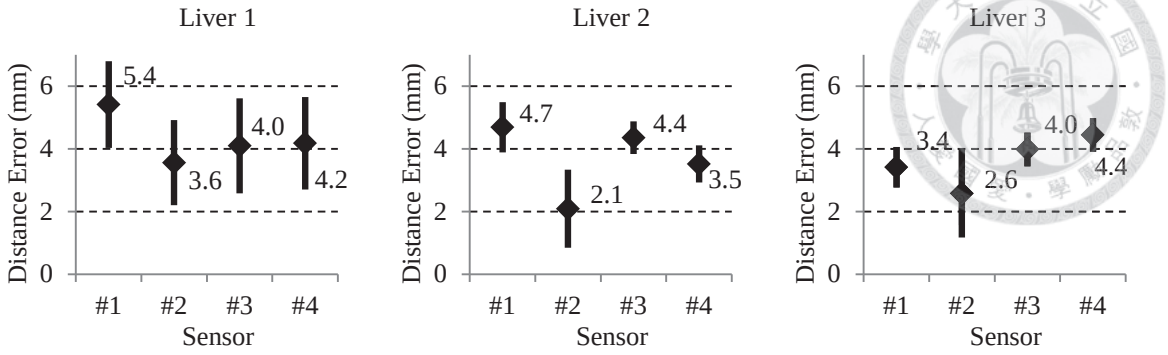

Figure 4.9 The results of the static localization experiment. Each center point is the mean of five repeated results at each sensor position. The bars show the range of the standard deviation at every sensor position.

Three axes were noted to identify the liver motion: the cranial-caudal direction (CC-dir.), the anterior-posterior direction (AP-dir.), and the left-right direction (LR-dir.). The localization errors along the three axes in the body were -0.02 ± 2.5 mm along the CC-dir., 0.3 ± 1.6 mm along the AP-dir., and 0.01 ± 2.9 mm along the LR-dir., respectively (shown in Figure 4.10). The results showed that the method had high accuracy for static tumor localization. However, the STD values of error, which was probably caused by difficulty of the image processing of the low quality and speckle noise affected ultrasound images, could be reduced by improvement of image processing.

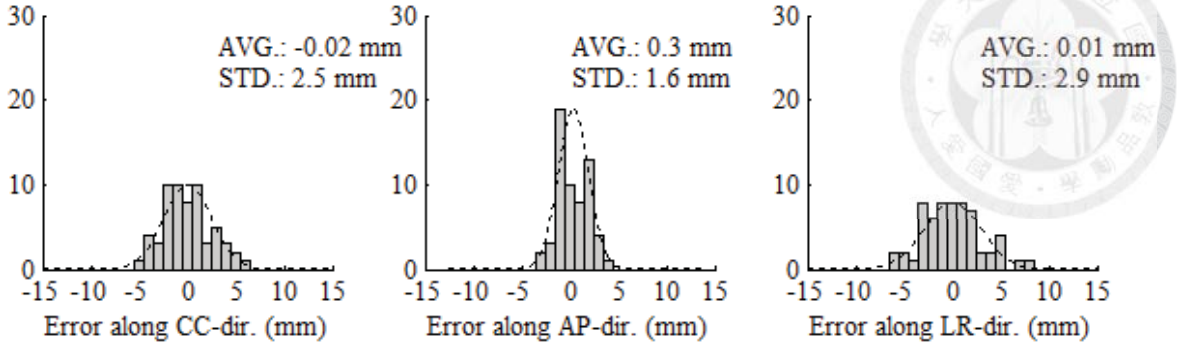

(a) (b) (c)

Figure 4.10 The static localization errors along the three axes of the body: (a) -0.02 ± 2.5 mm along the CC-dir., (b) 0.3 ± 1.6 mm along the AP-dir., and (c) is 0.01 ± 2.9 mm along the LR-dir..

4.3.2 Real-Time Tracking

In real-time tracking, the motion of the pig liver phantom was a wave with a 30 mm amplitude and a 6 sec period imitating human respiration, while the motion occurred along the CC-dir. as shown in Figure 4.11. The tracking error was 5.1 ± 2.4 mm in the range from 3.4 to 13.5 mm. The computing time was around 0.2 sec (5 Hz sampling rate), which is 10 times faster than the average human respiration period. Both the mean and standard deviations of each sensor in the tracking experiment were larger than those in the static localization experiment. The errors were 3.8 ± 4.1 mm along the CC-dir., -0.6 ± 1.2 mm along the AP-dir., and -0.5 ± 1.2 mm along the LR-dir., respectively, as shown in Figure 4.12. It showed high accuracy in the AP-LR plane (the CT slices).

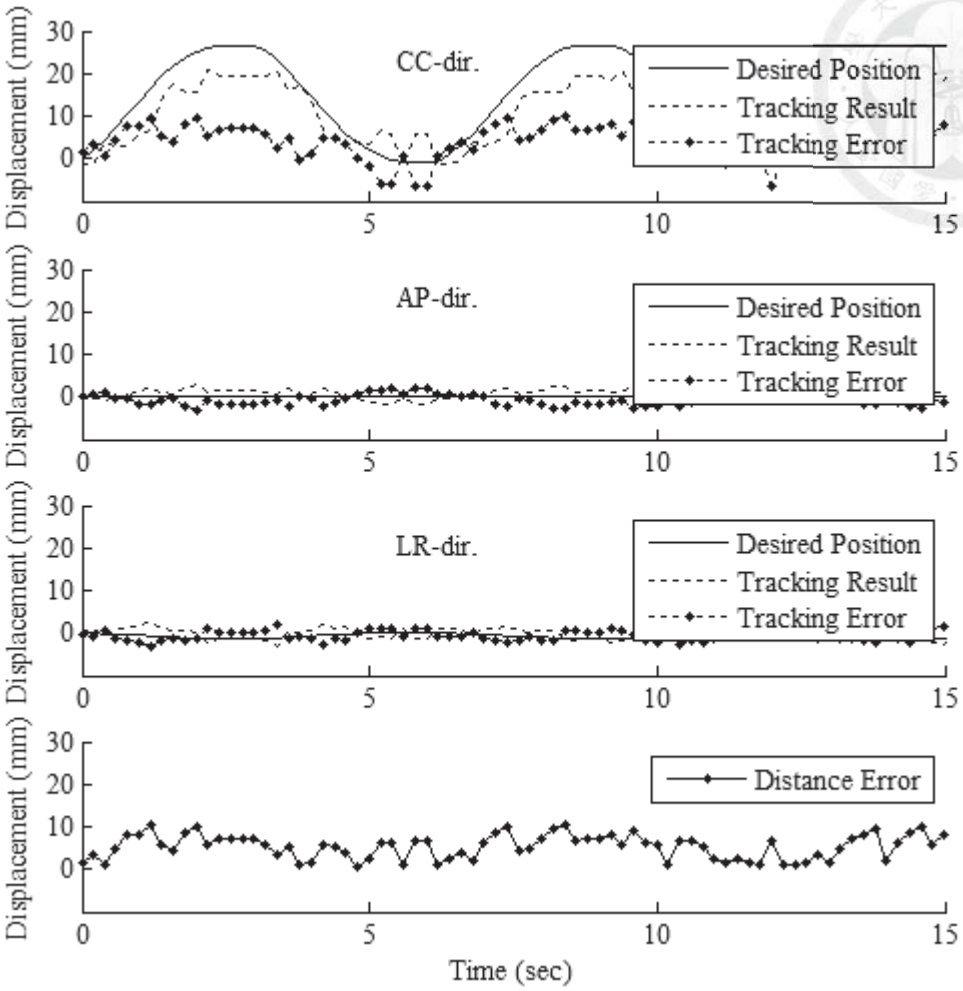

Figure 4.11 The phantom motion, tracking result, and the tracking error along the three body axes.

The tracking errors along the CC-dir. (main movement direction) were larger than that along the other directions. The errors were supposedly caused by the computing time and the image registration. The maximum displacement of the phantom along the CC-dir. was about 13 mm in one computing time. This factor called ‘one-step delay’ was the probable cause of the error along the CC-dir. The tracking accuracy can be enhanced by reducing the computing time and predicting the next position using

historical information. Moreover, the speckle noise in the ultrasound image might have affected the results from the liver segmentation. Incorrect segmentation reduces the accuracy of image registration and causes the error in the image plane (AP-LR plane). To improve the registration accuracy, contrast enhanced ultrasound should be used to reduce the noise effect.

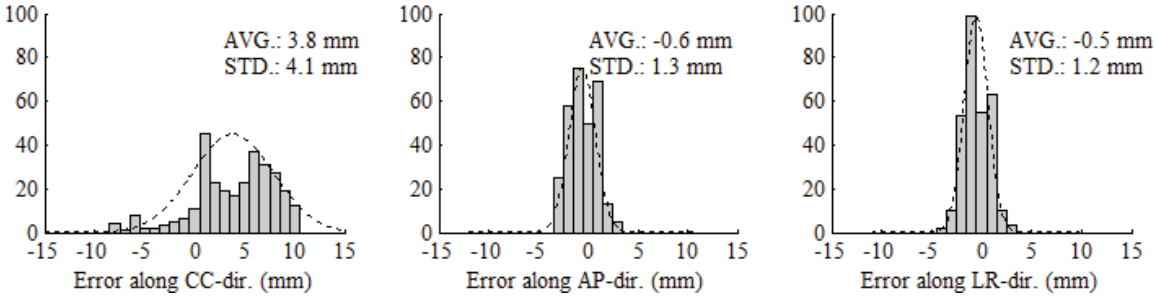

(a) (b) (c)

Figure 4.12 The real-time tracking error: (a) 3.8 ± 4.1 mm along the CC-dir., (b) -0.6 ± 1.3 mm along the AP-dir., and (c) -0.5 ± 1.2 mm along the LR-dir..

Table 4.1 Results from the in phantom experiment

Error	CC-dir.	AP-dir.	LR-dir.	Distance
Static Localization	-0.02 ± 2.5	0.3 ± 1.6	0.01 ± 2.9	3.8 ± 1.6
Real-Time Tracking	3.8 ± 4.1	-0.6 ± 1.3	-0.5 ± 1.2	5.1 ± 2.4

Average ± STD (Unit: mm)

4.4 Discussions and Summary

In this study, a new liver tumor tracking approach is proposed. It uses tracked ultrasound with CT image registration for real-time liver tumor tracking. In other words, the tumor location can be detected without scanning the tumor directly by tracked ultrasound. This approach solves two issues: the location of tumor might be lost (1) when it is hidden in the rib shadow where is an echo-undetectable area and (2) when it leaves the scanning area of the tracked ultrasound. The proposed approach integrates preoperative CT scan and intraoperative tracked ultrasound to estimate the tumor location. The accuracy of this approach is 3.8 ± 1.6 mm for static localization and 5.1 ± 2.4 mm for real-time tracking.

So far, little research has been done to real-time track liver tumors using tracked ultrasound with CT/MRI image registration. Mercier *et al.* presented a navigation system using tracked ultrasound and MRI image registration for brain-shift detection during neurosurgery. In that study, the MRI image was calibrated with landmarks of patients, and vessel-based and mutual-information techniques were used in MRI-ultrasound image registration. The error in MRI-ultrasound registration was 6.1 ± 3.4 mm under over 300 sec computation time [68]. In 2011, Lang *et al.* proposed a localization method using CT-ultrasound registration with contour features, and the tracking accuracy was 2.6 mm [78]. Gill *et al.* used CT-ultrasound registration to

localize the lumbar spine in 2012. The localization error was 1.7 ± 0.39 mm with 11 sec run time [93].

According to the above researches, all of them discussed static localization, and none of them used image registration to track liver tumors in real-time. In our study, the proposed approach has shortest rum time (around 0.2 sec) so that it can track liver tumors in near real-time. In the future, the accuracy of the proposed approach will be improved and tested on animal models with implanted liver tumors.

Table 4.2 Comparison of tracking results.

	Feature	Run time (sec)	Localization error (mm)	Tracking error (mm)
Mercier *et al.* [68]	Landmark	> 300	6.1 ± 3.4	Not analysis
Lang *et al.* [78]	Contour	0.5	2.6	Not analysis
Gill *et al.* [93]	Contour	11	1.7 ± 0.39	Not analysis
Our work	Contour	0.2	3.8 ± 1.6	5.1 ± 2.4

Average ± STD

Chapter 5 Conclusions and Future Work

Two liver tumor tracking methods are proposed in this dissertation: (1) surrogate-based tracking with end-points registration and (2) tracked ultrasound tracking with CT-ultrasound image registration.

In the surrogate-based tracking, effectiveness of external surrogates and performance image-to-physical registration were verified. The results show that:

(1) Abdominal wall displacement has a high relationship with liver tumor movement.

(2) Upper abdomen produces good performance for liver motion estimation, and the best place to obtain external signals is at the middle of upper abdomen.

(3) Multiple surrogates have benefit to provide better performance than singular surrogate does.

(4) The estimation model can maintain the accuracy for at least 10 minutes.

(5) External markers provide actual liver tumor position from CT images.

A novel tracked ultrasound tracking approach with image registration is first proposed for real-time liver tumor tracking. This method has not been used to track liver tumor in real time. A phantom experiment was conducted to validate the tracking performance of the proposed method. The results show that:

(1) Tumor position can be tracked by integrating liver positon tracked by ultrasound and tumor relative position from CT image.

(2) Ultrasound probe alignment and image registration reduce the run time to achieve real-time tracking (around 5 Hz).

In the future, two issues would be considered: (1) image processing in ultrasound images and (2) tumor motion prediction. Ultrasound image processing affects directly the performance of image registration. Improvement of image processing can enhance the tracking accuracy. Due to the trade-off between the run time and accuracy in real-time tracking, prediction is one of methods to enhance the tracking accuracy without reducing run time. The proposed methods have potential to serve as guidance in radiotherapy and thermotherapy for real-time liver tumor treatment.

References

[1] J. Ferlay, H.-R. Shin, F. Bray, D. Forman, C. Mathers, and D. M. Parkin, "Estimates of Worldwide Burden of Cancer in 2008: Globocan 2008," *International Journal of Cancer,* vol. 127, pp. 2893-2917, 2010.

[2] A. Jemal, F. Bray, M. M. Center, J. Ferlay, E. Ward, and D. Forman, "Global Cancer Statistics," *Cancer Journal for Clinicians,* vol. 61, pp. 69-90, 2011.

[3] H. Kaneko, S. Takagi, Y. Otsuka, M. Tsuchiya, A. Tamura, T. Katagiri, T. Maeda, and T. Shiba, "Laparoscopic Liver Resection of Hepatocellular Carcinoma," *The American Journal of Surgery,* vol. 189, pp. 190-194, 2005.

[4] G. Belli, P. Limongelli, C. Fantini, A. D'Agostino, L. Cioffi, A. Belli, and G. Russo, "Laparoscopic and Open Treatment of Hepatocellular Carcinoma in Patients with Cirrhosis," *British Journal of Surgery,* vol. 96, pp. 1041-1048, 2009.

[5] "民國 102 年全國主要死亡原因," 中華民國行政院衛生福利部 2014.

[6] "全國主要癌症死亡原因," 中華民國行政院衛生福利部 2014.

[7] A. Laurent, D. Cherqui, M. Lesurtel, F. Brunetti, C. Tayar, and P. L. Fagniez, "Laparoscopic Liver Resection for Subcapsular Hepatocellular Carcinoma Complicating Chronic Liver Disease," *Archives of Surgery,* vol. 138, pp. 763-769, 2003.

[8] H. Tranchart, G. Di Giuro, P. Lainas, J. Roudie, H. Agostini, D. Franco, and I.

Dagher, "Laparoscopic Resection for Hepatocellular Carcinoma: A Matched-Pair Comparative Study," *Surgical Endoscopy,* vol. 24, pp. 1170-1176, 2010.

[9] M. J. Murphy, "Tracking Moving Organs in Real Time," *Seminars in Radiation Oncology,* vol. 14, pp. 91-100, 2004.

[10] T. J. Dubinsky, C. Cuevas, M. K. Dighe, O. Kolokythas, and J. H. Hwang, "High-Intensity Focused Ultrasound: Current Potential and Oncologic Applications," *American Journal of Roentgenology,* vol. 190, pp. 191-199, 2008.

[11] Y. F. Zhou, "High Intensity Focused Ultrasound in Clinical Tumor Ablation," *World Journal of Clinical Oncology,* vol. 2, pp. 8-27, 2011.

[12] A. Muacevic, B. Wowra, and M. Reiser, "Cyberknife: Review of First 1,000 Cases at a Dedicated Therapy Center," *Int. J. Computer Assisted Radiology and Surgery,* vol. 3, pp. 447-456, 2008.

[13] T. E. Schefter, B. D. Kavanagh, R. D. Timmerman, H. R. Cardenes, A. Baron, and L. E. Gaspar, "A Phase I Trial of Stereotactic Body Radiation Therapy (SBRT) for Liver Metastases," *International Journal of Radiation Oncology*Biology*Physics,* vol. 62, pp. 1371-1378, 2005.

[14] R. D. Timmerman, B. D. Kavanagh, L. C. Cho, L. Papiez, and L. Xing, "Stereotactic Body Radiation Therapy in Multiple Organ Sites," *Journal of Clinical Oncology,* vol. 25, pp. 947-952, 2007.

[15] Q. J. Wu, D. Thongphiew, W. Zhiheng, V. Chankong, and Y. Fangfang, "The Impact of Respiratory Motion and Treatment Technique on Stereotactic Body Radiation Therapy for Liver Cancer," *Medical Physics*, vol. 35, pp. 1440-1451, 2008.

[16] H. Zhong, T. Kanade, and D. Schwartzman, "Image Thickness Correction for Navigation with 3D Intra-Cardiac Ultrasound Catheter," presented at the Medical Image Computing and Computer-Assisted Intervention - MICCAL 2008, pp. 485-92, 2008.

[17] P. Weiss, J. Baker, and E. Potchen, "Assessment of Hepatic Respiratory Excursion," *Journal of Nuclear Medicine*, vol. 13, pp. 758-759, 1972.

[18] S. C. Davies, A. L. Hill, R. B. Holmes, M. Halliwell, and P. C. Jackson, "Ultrasound Quantitation of Respiratory Organ Motion in the Upper Abdomen," *British Journal of Radiology*, vol. 67, pp. 1096-1102, 1994.

[19] K. M. Langen and D. T. L. Jones, "Organ Motion and Its Management," *International Journal of Radiation Oncology*Biology*Physics*, vol. 50, pp. 265-278, 2001.

[20] B. Bussels, L. Goethals, M. Feron, D. Bielen, S. Dymarkowski, P. Suetens, and K. Haustermans, "Respiration-Induced Movement of the Upper Abdominal Organs: A Pitfall for the Three-Dimensional Conformal Radiation Treatment of Pancreatic

Cancer," *Radiotherapy and Oncology*, vol. 68, pp. 69-74, 2003.

[21] H. Wu, G. C. Sharp, B. Salzberg, D. Kaeli, H. Shirato, and S. B. Jiang, "A Finite State Model for Respiratory Motion Analysis in Image Guided Radiation Therapy," *Physics in Medicine and Biology*, vol. 49, pp. 5357-5372, 2004.

[22] Y. Tsunashima, T. Sakae, Y. Shioyama, K. Kagei, T. Terunuma, A. Nohtomi, and Y. Akine, "Correlation between the Respiratory Waveform Measured Using a Respiratory Sensor and 3D Tumor Motion in Gated Radiotherapy," *International Journal of Radiation Oncology*Biology*Physics*, vol. 60, pp. 951-958, 2004.

[23] J. M. Balter, R. K. Ten Haken, T. S. Lawrence, K. L. Lam, and J. M. Robertson, "Uncertainties in CT-Based Radiation Therapy Treatment Planning Associated with Patient Breathing," *International Journal of Radiation Oncology*Biology*Physics*, vol. 36, pp. 167-174, 1996.

[24] K. Kitamura, H. Shirato, Y. Seppenwoolde, T. Shimizu, Y. Kodama, H. Endo, R. Onimaru, M. Oda, K. Fujita, S. Shimizu, and K. Miyasaka, "Tumor Location, Cirrhosis, and Surgical History Contribute to Tumor Movement in the Liver, as Measured During Stereotactic Irradiation Using a Real-Time Tumor-Tracking Radiotherapy System," *International Journal of Radiation Oncology*Biology*Physics*, vol. 56, pp. 221-228, 2003.

[25] H. Shirato, S. Shimizu, K. Kitamura, and R. Onimaru, "Organ Motion in

Image-Guided Radiotherapy: Lessons from Real-Time Tumor-Tracking Radiotherapy," *International Journal of Clinical Oncology,* vol. 12, pp. 8-16, 2007.

[26] D. P. Gierga, J. Brewer, G. C. Sharp, M. Betke, C. G. Willett, and G. T. Chen, "The Correlation between Internal and External Markers for Abdominal Tumors: Implications for Respiratory Gating," *International Journal of Radiation Oncology*Biology*Physics,* vol. 61, pp. 1551-1558, 2005.

[27] A. S. Beddar, K. Kainz, T. M. Briere, Y. Tsunashima, T. Pan, K. Prado, R. Mohan, M. Gillin, and S. Krishnan, "Correlation between Internal Fiducial Tumor Motion and External Marker Motion for Liver Tumors Imaged with 4D-CT," *International Journal of Radiation Oncology*Biology*Physics,* vol. 67, pp. 630-638, 2007.

[28] H. Shirato, Y. Seppenwoolde, K. Kitamura, R. Onimura, and S. Shimizu, "Intrafractional Tumor Motion: Lung and Liver," *Seminars in Radiation Oncology,* vol. 14, pp. 10-8, 2004.

[29] A. Kirilova, G. Lockwood, P. Choi, N. Bana, M. A. Haider, K. K. Brock, C. Eccles, and L. A. Dawson, "Three-Dimensional Motion of Liver Tumors Using Cine-Magnetic Resonance Imaging," *International Journal of Radiation Oncology*Biology*Physics,* vol. 71, pp. 1189-1195, 2008.

[30] S. S. Vedam, P. J. Keall, V. R. Kini, and R. Mohan, "Determining Parameters for Respiration-Gated Radiotherapy," *Med. Phys.,* vol. 28, pp. 2139-2146, 2001.

[31] Y. Seppenwoolde, H. Shirato, K. Kitamura, S. Shimizu, M. van Herk, J. V. Lebesque, and K. Miyasaka, "Precise and Real-Time Measurement of 3D Tumor Motion in Lung Due to Breathing and Heartbeat, Measured During Radiotherapy," *International Journal of Radiation Oncology*Biology*Physics,* vol. 53, pp. 822-834, 2002.

[32] H. D. Kubo and B. C. Hill, "Respiration Gated Radiotherapy Treatment: A Technical Study," *Physics in Medicine and Biology,* vol. 41, pp. 83-91, 1996.

[33] H. D. Kubo, P. M. Len, S. i. Minohara, and H. Mostafavi, "Breathing-Synchronized Radiotherapy Program at the University of California Davis Cancer Center," *Medical Physics,* vol. 27, pp. 346-353, 2000.

[34] S. Hunjan, G. Starkschall, K. Prado, L. Dong, and P. Balter, "Lack of Correlation between External Fiducial Positions and Internal Tumor Positions During Breath-Hold CT," *Int. J. Radiat. Oncol. Biol. Phys.,* vol. 76, pp. 1586-1591, 2010.

[35] I. C. Laura, A. K. Y. Chao, A. Sandhu, and S. B. Jiang, "The Diaphragm as an Anatomic Surrogate for Lung Tumor Motion," *Physics in Medicine and Biology,* vol. 54, pp. 3529-3541, 2009.

[36] S. S. Vedam, V. R. Kini, P. J. Keall, V. Ramakrishnan, H. Mostafavi, and R.

Mohan, "Quantifying the Predictability of Diaphragm Motion During Respiration with a Noninvasive External Marker," *Med. Phys.*, vol. 30, pp. 505-513, 2003.

[37] J. D. P. Hoisak, K. E. Sixel, R. Tirona, P. C. F. Cheung, and J.-P. Pignol, "Correlation of Lung Tumor Motion with External Surrogate Indicators of Respiration," *International Journal of Radiation Oncology*Biology*Physics*, vol. 60, pp. 1298-1306, 2004.

[38] T. Zhang, H. Keller, M. J. O'Brien, T. R. Mackie, and B. Paliwal, "Application of the Spirometer in Respiratory Gated Radiotherapy," *Medical Physics*, vol. 30, pp. 3165-3171, 2003.

[39] T. Kimura, Y. Hirokawa, Y. Murakami, M. Tsujimura, T. Nakashima, Y. Ohno, M. Kenjo, Y. Kaneyasu, K. Wadasaki, and K. Ito, "Reproducibility of Organ Position Using Voluntary Breath-Hold Method with Spirometer for Extracranial Stereotactic Radiotherapy," *International Journal of Radiation Oncology*Biology*Physics*, vol. 60, pp. 1307-1313, 2004.

[40] K. T. Malinowski, J. R. Pantarotto, S. Senan, T. J. McAvoy, and W. D. D'Souza, "Inferring Positions of Tumor and Nodes in Stage III Lung Cancer from Multiple Anatomical Surrogates Using Four-Dimensional Computed Tomography," *Int. J. Radiat. Oncol. Biol. Phys.*, vol. 77, pp. 1553-1560, 2010.

[41] H. Yan, F. Yin, G. Zhu, M. Ajlouni, and J. H. Kim, "The Correlation Evaluation of

a Tumor Tracking System Using Multiple External Markers," *Medical Physics*, vol. 33, pp. 4073-4084, 2006.

[42] B. Cho, P. R. Poulsen, A. Sawant, D. Ruan, and P. J. Keall, "Real-Time Target Position Estimation Using Stereoscopic Kilovoltage/Megavoltage Imaging and External Respiratory Monitoring for Dynamic Multileaf Collimator Tracking," *International Journal of Radiation Oncology*Biology*Physics*, vol. 79, pp. 269-278, 2011.

[43] K. Malinowski, T. J. McAvoy, R. George, S. Dietrich, and W. D. D'Souza, "Incidence of Changes in Respiration-Induced Tumor Motion and Its Relationship with Respiratory Surrogates During Individual Treatment Fractions," *Int. J. Radiat. Oncol. Biol. Phys.*, vol. 82, pp. 1665-1673, 2012.

[44] M. Nakamura, Y. Narita, Y. Matsuo, M. Narabayashi, M. Nakata, A. Sawada, T. Mizowaki, Y. Nagata, and M. Hiraoka, "Effect of Audio Coaching on Correlation of Abdominal Displacement with Lung Tumor Motion," *Int. J. Radiat. Oncol. Biol. Phys.*, vol. 75, pp. 558-563, 2009.

[45] Z. Yaniv and K. Cleary, "Fluoroscopy Based Accuracy Assessment of Electromagnetic Tracking," pp. 61410L-61410L-7, 2006.

[46] G. Imai, H. Takahata, and M. Okada, "Particle Filter Assisted Rfid Tag Location Method for Surgery Support System," in *7th International Symposium on Medical*

Information and Communication Technology (ISMICT), pp. 135-138, 2013.

[47] X. Tang, G. C. Sharp, and S. B. Jiang, "Fluoroscopic Tracking of Multiple Implanted Fiducial Markers Using Multiple Object Tracking," *Physics in Medicine and Biology*, vol. 52, pp. 4081-98, 2007.

[48] H. Shirato, S. Shimizu, T. Kunieda, K. Kitamura, M. van Herk, K. Kagei, T. Nishioka, S. Hashimoto, K. Fujita, H. Aoyama, K. Tsuchiya, K. Kudo, and K. Miyasaka, "Physical Aspects of a Real-Time Tumor-Tracking System for Gated Radiotherapy," *International Journal of Radiation Oncology*Biology*Physics*, vol. 48, pp. 1187-1195, 2000.

[49] S. Shimizu, H. Shirato, S. Ogura, H. Akita-Dosaka, K. Kitamura, T. Nishioka, K. Kagei, M. Nishimura, and K. Miyasaka, "Detection of Lung Tumor Movement in Real-Time Tumor-Tracking Radiotherapy," *International Journal of Radiation Oncology*Biology*Physics*, vol. 51, pp. 304-310, 2001.

[50] P. J. Keall, S. Joshi, S. S. Vedam, J. V. Siebers, V. R. Kini, and R. Mohan, "Four-Dimensional Radiotherapy Planning for DMLC-Based Respiratory Motion Tracking," *Medical Physics*, vol. 32, pp. 942-951, 2005.

[51] D. J. Grand, M. A. Atalay, J. J. Cronan, W. W. Mayo-Smith, and D. E. Dupuy, "CT-Guided Percutaneous Lung Biopsy: Comparison of Conventional CT Fluoroscopy to CT Fluoroscopy with Electromagnetic Navigation System in 60

Consecutive Patients," *European Journal of Radiology,* vol. 79, pp. e133-e136, 2011.

[52] M. M. Coselmon, J. M. Balter, D. L. McShan, and M. L. Kessler, "Mutual Information Based CT Registration of the Lung at Exhale and Inhale Breathing States Using Thin-Plate Splines," *Medical Physics,* vol. 31, pp. 2942-2948, 2004.

[53] J. R. McClelland, J. M. Blackall, S. g. n. Tarte, A. C. Chandler, S. Hughes, S. Ahmad, D. B. Landau, and D. J. Hawkes, "A Continuous 4D Motion Model from Multiple Respiratory Cycles for Use in Lung Radiotherapy," *Medical Physics,* vol. 33, p. 3348, 2006.

[54] H. Handels, R. Werner, R. Schmidt, T. Frenzel, W. Lu, D. Low, and J. Ehrhardt, "4D Medical Image Computing and Visualization of Lung Tumor Mobility in Spatio-Temporal CT Image Data," *International Journal of Medical Informatics,* vol. 76, pp. S433-S439, 2007.

[55] M. Fusari, S. Maurea, M. Imbriaco, C. Mollica, G. Avitabile, F. Soscia, L. Camera, and M. Salvatore, "Comparison between Multislice CT and MR Imaging in the Diagnostic Evaluation of Patients with Pancreatic Masses," *La Radiologia Medica,* vol. 115, pp. 453-466, 2010.

[56] S. Shimizu, H. Shirato, B. Xo, K. Kagei, T. Nishioka, S. Hashimoto, K. Tsuchiya, H. Aoyama, and K. Miyasaka, "Three-Dimensional Movement of a Liver Tumor

Detected by High-Speed Magnetic Resonance Imaging," *Radiotherapy and Oncology,* vol. 50, pp. 367-370, 1999.

[57] J. Tokuda, S. Morikawa, T. Dohi, and N. Hata, "Motion Tracking in MR-Guided Liver Therapy by Using Navigator Echoes and Projection Profile Matching1," *Academic Radiology,* vol. 11, pp. 111-120, 2004.

[58] L. Jan, J. Tokuda, R. Kikinis, C. Burghart, and N. Hata, "A Device Guidance Method for Organ Motion Compensation in MRI-Guided Therapy," *Physics in Medicine and Biology,* vol. 52, pp. 6427-6438, 2007.

[59] T. Rohlfing, C. R. Maurer, W. G. O'Dell, and J. Zhong, "Modeling Liver Motion and Deformation During the Respiratory Cycle Using Intensity-Based Nonrigid Registration of Gated MR Images," *Medical Physics,* vol. 31, pp. 427-432, 2004.

[60] F. M. Fennessy, K. Tuncali, P. R. Morrison, and C. M. Tempany, "Magnetic Resonance Imaging-Guided Interventions in the Genitourinary Tract: An Evolving Concept," *Radiologic Clinics of North America,* vol. 46, pp. 149-66, vii, 2008.

[61] C. L. Eccles, R. Patel, A. K. Simeonov, G. Lockwood, M. Haider, and L. A. Dawson, "Comparison of Liver Tumor Motion with and without Abdominal Compression Using Cine-Magnetic Resonance Imaging," *International Journal of Radiation Oncology*Biology*Physics,* vol. 79, pp. 602-608, 2011.

[62] B. D. de Senneville, C. Mougenot, and C. T. Moonen, "Real-Time Adaptive

Methods for Treatment of Mobile Organs by MRI-Controlled High-Intensity Focused Ultrasound," *Magnetic Resonance in Medicine*, vol. 57, pp. 319-30, 2007.

[63] B. E. O'Neill, C. Karmonik, E. Sassaroli, and K. C. Li, "Estimation of Thermal Dose from MR Thermometry During Application of Nonablative Pulsed High Intensity Focused Ultrasound," *Journal of Magnetic Resonance Imaging*, vol. 35, pp. 1169-1178, 2012.

[64] R. W. Prager, R. N. Rohling, A. H. Gee, and L. Berman, "Rapid Calibration for 3-D Freehand Ultrasound," *Ultrasound in Medicine & Biology*, vol. 24, pp. 855-869, 1998.

[65] H. Guo, S. Deng, L. Jiang, Y. Cao, J. Zhang, H. Zheng, and Q. Ding, "Variational Approach to Reconstruct Surface from Sparse and Nonparallel Contours in Freehand 3D Ultrasound Imaging," vol. 8335, pp. 83351V-1-8, 2012.

[66] W. Y. Zhang, R. N. Rohling, and D. K. Pai, "Surface Extraction with a Three-Dimensional Freehand Ultrasound System," *Ultrasound in Medicine & Biology*, vol. 30, pp. 1461-1473, 2004.

[67] G. P. Penney, J. M. Blackall, M. S. Hamady, T. Sabharwal, A. Adam, and D. J. Hawkes, "Registration of Freehand 3D Ultrasound and Magnetic Resonance Liver Images," *Medical Image Analysis*, vol. 8, pp. 81-91, 2004.

[68] L. Mercier, R. F. Del Maestro, K. Petrecca, A. Kochanowska, S. Drouin, C. X. Yan, A. L. Janke, S. J. Chen, and D. L. Collins, "New Prototype Neuronavigation System Based on Preoperative Imaging and Intraoperative Freehand Ultrasound: System Description and Validation," *International Journal of Computer Assisted Radiology and Surgery,* vol. 6, pp. 507-522, 2011.

[69] J. Wu, C. Li, S. Huang, F. Liu, B. Tan, L. Ooi, H. Yu, and J. Liu, "Fast and Robust Extraction of Surrogate Respiratory Signal from Intra-Operative Liver Ultrasound Images," *International Journal of Computer Assisted Radiology and Surgery,* vol. 8, pp. 1027-1035, 2013.

[70] S. S. Vedam, V. R. Kini, P. J. Keall, V. Ramakrishnan, H. Mostafavi, and R. Mohan, "Quantifying the Predictability of Diaphragm Motion During Respiration with a Noninvasive External Marker," *Medical Physics,* vol. 30, pp. 505-513, 2003.

[71] M. Hoogeman, J. B. Prevost, J. Nuyttens, J. Poll, P. Levendag, and B. Heijmen, "Clinical Accuracy of the Respiratory Tumor Tracking System of the Cyberknife: Assessment by Analysis of Log Files," *International Journal of Radiation Oncology*Biology*Physics*, vol. 74, pp. 297-303, 2009.

[72] S. Ahn, "A Feasibility Study on the Prediction of Tumour Location in the Lung from Skin Motion," *British Journal of Radiology,* vol. 77, pp. 588-596, 2004.

[73] M. Nakamura, Y. Narita, Y. Matsuo, M. Narabayashi, M. Nakata, A. Sawada, T. Mizowaki, Y. Nagata, and M. Hiraoka, "Effect of Audio Coaching on Correlation of Abdominal Displacement with Lung Tumor Motion," *International Journal of Radiation Oncology*Biology*Physics*, vol. 75, pp. 558-563, 2009.

[74] M. Feng, J. M. Balter, D. Normolle, S. Adusumilli, Y. Cao, T. L. Chenevert, and E. Ben-Josef, "Characterization of Pancreatic Tumor Motion Using Cine MRI: Surrogates for Tumor Position Should Be Used with Caution," *International Journal of Radiation Oncology*Biology*Physics*, vol. 74, pp. 884-891, 2009.

[75] R. H. Abhilash and S. Chauhan, "Respiration-Induced Movement Correlation for Synchronous Noninvasive Renal Cancer Surgery," *IEEE Trans Ultrason Ferroelectr Freq Control*, vol. 59, pp. 1478-86, 2012.

[76] D. Yeung, J. Palta, J. Fontanesi, and L. Kun, "Systematic Analysis of Errors in Target Localization and Treatment Delivery in Stereotactic Radiosurgery (SRS)," *International Journal of Radiation Oncology*Biology*Physics*, vol. 28, pp. 493-498, 1994.

[77] K. Kagawa, W. R. Lee, T. E. Schultheiss, M. A. Hunt, A. H. Shaer, and G. E. Hanks, "Initial Clinical Assessment of CT-MRI Image Fusion Software in Localization of the Prostate for 3D Conformal Radiation Therapy," *International Journal of Radiation Oncology*Biology*Physics*, vol. 38, pp. 319-325, 1997.

[78] P. Lang, E. C. S. Chen, G. M. Guiraudon, D. L. Jones, D. Bainbridge, M. W. Chu, M. Drangova, N. Hata, A. Jain, and T. M. Peters, "Feature-Based US to CT Registration of the Aortic Root," pp. 79641G-1-9, 2011.

[79] S. Weisberg, *Applied Linear Regression*, 3rd ed. Hoboken, New Jersey: John Wiley & Sons, Inc., 2005.

[80] K. H. Chang, M. C. Ho, C. C. Yeh, Y. C. Chen, F. L. Lian, W. L. Lin, J. Y. Yen, and Y. Y. Chen, "Effectiveness of External Respiratory Surrogates for in Vivo Liver Motion Estimation," *Medical Physics*, vol. 39, pp. 5293-5301, 2012.

[81] K. K. Ng, R. T. Poon, S. C. Chan, K. S. Chok, T. T. Cheung, H. Tung, F. Chu, W. K. Tso, W. C. Yu, C. M. Lo, and S. T. Fan, "High-Intensity Focused Ultrasound for Hepatocellular Carcinoma: A Single-Center Experience," *Annals of Surgery*, vol. 253, pp. 981-986, 2011.

[82] L. Vincent and P. Soille, "Watersheds in Digital Spaces: An Efficient Algorithm Based on Immersion Simulations," *IEEE Transactions on Pattern Analysis and Machine Intelligence*, vol. 13, pp. 583-598, 1991.

[83] P. W. Hsu, R. Prager, A. Gee, and G. Treece, "Freehand 3D Ultrasound Calibration: A Review," *Advanced Imaging in Biology and Medicine*, pp. 47-84, 2009.

[84] C. Bergmeir, M. Seitel, C. Frank, R. De Simone, H. P. Meinzer, and I. Wolf, "Comparing Calibration Approaches for 3D Ultrasound Probes," *International*

Journal of Computer Assisted Radiology and Surgery, vol. 4, pp. 203-213, 2009.

[85] G. Carbajal, A. Lasso, Á. Gómez, and G. Fichtinger, "Improving N-Wire Phantom-Based Freehand Ultrasound Calibration," *International Journal of Computer Assisted Radiology and Surgery,* vol. 8, pp. 1063-1072, 2013.

[86] H. Zhang, F. Banovac, A. White, and K. Cleary, "Freehand 3D Ultrasound Calibration Using an Electromagnetically Tracked Needle," presented at the Medical Imaging 2006: Visualization, Image-Guided Procedures, and Display, San Diego, CA, pp. 61412M1-9, 2006.

[87] E. Melvær, K. Mørken, and E. Samset, "A Motion Constrained Cross-Wire Phantom for Tracked 2D Ultrasound Calibration," *International Journal of Computer Assisted Radiology and Surgery,* vol. 7, pp. 611-620, 2012.

[88] D. L. G. Hill, P. G. Batchelor, M. Holden, and D. J. Hawkes, "Medical Image Registration," *Physics in Medicine and Biology,* vol. 46, pp. R1-R45, 2001.

[89] A. Leroy, P. Mozer, Y. Payan, and J. Troccaz, "Rigid Registration of Freehand 3D Ultrasound and CT-Scan Kidney Images," presented at the Medical Image Computing and Computer-Assisted Intervention - MICCAI 2004, pp. 837-844, 2004.

[90] A. Leroy, P. Mozer, Y. Payan, and J. Troccaz, "Intensity-Based Registration of Freehand 3D Ultrasound and CT-Scan Images of the Kidney," *International*

Journal of Computer Assisted Radiology and Surgery, vol. 2, pp. 31-41, 2007.

[91] X. Lijian, L. Jun, Z. Weiwei, and G. Lixu, "A Novel Algorithm for CT-Ultrasound Registration," in *2013 IEEE Point-of-Care Healthcare Technologies (PHT)*, pp. 101-104, 2013.

[92] J. P. Lewis, "Fast Normalized Cross-Correlation," *Vision Interface*, pp. 120-123, 1995.

[93] S. Gill, P. Abolmaesumi, G. Fichtinger, J. Boisvert, D. Pichora, D. Borshneck, and P. Mousavi, "Biomechanically Constrained Groupwise Ultrasound to CT Registration of the Lumbar Spine," *Medical Image Analysis*, vol. 16, pp. 662-674, 2012.